

REPORT DOCUMENTATION PAGE			Form Approved OMB NO. 0704-0188		
<p>The public reporting burden for this collection of information is estimated to average 1 hour per response, including the time for reviewing instructions, searching existing data sources, gathering and maintaining the data needed, and completing and reviewing the collection of information. Send comments regarding this burden estimate or any other aspect of this collection of information, including suggestions for reducing this burden, to Washington Headquarters Services, Directorate for Information Operations and Reports, 1215 Jefferson Davis Highway, Suite 1204, Arlington VA, 22202-4302. Respondents should be aware that notwithstanding any other provision of law, no person shall be subject to any penalty for failing to comply with a collection of information if it does not display a currently valid OMB control number.</p> <p>PLEASE DO NOT RETURN YOUR FORM TO THE ABOVE ADDRESS.</p>					
1. REPORT DATE (DD-MM-YYYY) 14-05-2015		2. REPORT TYPE Final Report		3. DATES COVERED (From - To) 1-Jul-2010 - 31-Aug-2014	
4. TITLE AND SUBTITLE Final Report: Deep-UV Emitters and Detectors Based on Lattice-Matched Cubic Oxide Semiconductors (4.2 Optoelectronics)			5a. CONTRACT NUMBER W911NF-10-1-0159		
			5b. GRANT NUMBER		
			5c. PROGRAM ELEMENT NUMBER 611102		
6. AUTHORS Winston Schoenfeld			5d. PROJECT NUMBER		
			5e. TASK NUMBER		
			5f. WORK UNIT NUMBER		
7. PERFORMING ORGANIZATION NAMES AND ADDRESSES University of Central Florida 12201 Research Parkway, Suite 501 Orlando, FL 32826 -3246			8. PERFORMING ORGANIZATION REPORT NUMBER		
9. SPONSORING/MONITORING AGENCY NAME(S) AND ADDRESS (ES) U.S. Army Research Office P.O. Box 12211 Research Triangle Park, NC 27709-2211			10. SPONSOR/MONITOR'S ACRONYM(S) ARO		
			11. SPONSOR/MONITOR'S REPORT NUMBER(S) 57345-EL.6		
12. DISTRIBUTION AVAILABILITY STATEMENT Approved for Public Release; Distribution Unlimited					
13. SUPPLEMENTARY NOTES The views, opinions and/or findings contained in this report are those of the author(s) and should not be construed as an official Department of the Army position, policy or decision, unless so designated by other documentation.					
14. ABSTRACT The program resulted in significant advancement in the growth of rocksalt oxide ternary semiconductors and demonstrated devices. Comprehensive studies were put forth on the interrelation of growth conditions with device performance, resulting in a deeper understanding of the optimized parameters for growth. Efforts led to significant increases in solar-blind detector responsivity (up to 0.1 A/W) with sub--nanosecond dark currents and adjustable band edges. Furthermore, the program resulted in 4 journal publications, 6					
15. SUBJECT TERMS Oxide Semiconductors, ultra-violet detectors, zinc oxide					
16. SECURITY CLASSIFICATION OF:			17. LIMITATION OF ABSTRACT UU	15. NUMBER OF PAGES	19a. NAME OF RESPONSIBLE PERSON Winston Schoenfeld
a. REPORT UU	b. ABSTRACT UU	c. THIS PAGE UU			19b. TELEPHONE NUMBER 407-823-6898

Report Title

Final Report: Deep-UV Emitters and Detectors Based on Lattice-Matched Cubic Oxide Semiconductors (4.2 Optoelectronics)

ABSTRACT

The program resulted in significant advancement in the growth of rocksalt oxide ternary semiconductors and demonstrated devices. Comprehensive studies

were put forth on the interrelation of growth conditions with device performance, resulting in a deeper understanding of the optimized parameters

for growth. Efforts led to significant increases in solar-blind detector responsivity (up to 0.1 A/W) with sub--nanoamp dark currents and adjustable band edge. Furthermore, the program resulted in 4 journal publications, 6 conference papers, 1 issued patent, and partial/full support for three graduate students who received their PhD degrees from CREOL.

Enter List of papers submitted or published that acknowledge ARO support from the start of the project to the date of this printing. List the papers, including journal references, in the following categories:

(a) Papers published in peer-reviewed journals (N/A for none)

<u>Received</u>	<u>Paper</u>
05/14/2012	2.00 M. Wei, R.C. Boutwell, A. Scheurer, J.W. Mares, W.V. Schoenfeld. Optical and structural properties of NiMgO thin films formed by sol-gel spin coating, Thin Solid Films, (04 2012): 0. doi: 10.1016/j.tsf.2012.02.065
09/26/2013	4.00 R. Casey Boutwell, Ming Wei, Winston V. Schoenfeld. The effect of oxygen flow rate and radio frequency plasma power on cubic ZnMgO ultraviolet sensors grown by plasma-enhanced molecular beam epitaxy, Applied Physics Letters, (07 2013): 31114. doi: 10.1063/1.4815995
09/26/2013	3.00 R. Casey Boutwell, Ming Wei, Winston V. Schoenfeld. The effect of substrate temperature and source flux on cubic ZnMgO UV sensors grown by plasma-enhanced molecular beam epitaxy, Applied Surface Science, (11 2013): 254. doi: 10.1016/j.apsusc.2013.07.090
TOTAL:	3

Number of Papers published in peer-reviewed journals:

(b) Papers published in non-peer-reviewed journals (N/A for none)

<u>Received</u>	<u>Paper</u>
07/19/2011	1.00 M. Wei, R. Coutwell, J. Mares, A. Scheurer, W. Schoenfeld. Bandgap engineering of sol-gel synthesized amorphous Zn _{1-x} Mg _x O films, Applied Physics Letters, (06 2011): . doi:
TOTAL:	1

Number of Papers published in non peer-reviewed journals:

(c) Presentations

[1] "Effect of Growth Conditions on Cubic ZnMgO films"; C. R. Boutwell, M. Wei, and W. V. Schoenfeld; in Proceedings of AVS-59, Tampa, FL, 2012.

[2] "Cubic ZnMgO and NiMgO for UV-C Applications"; R. C. Boutwell, J. W. Mares, M. W. Wei, and W. V. Schoenfeld; in Proceedings of AVS-58, Nashville, TN, 2011.

[3] "Effect of Growth Conditions on Cubic ZnMgO films"; C. R. Boutwell, M. Wei, and W. V. Schoenfeld; presented at FL-AVS Symposium, Thin Films Growth and Characterization I Session, Orlando, FL, 2012.

[4] "Oxide Semiconductors for Ultra-violet Optoelectronics"; W. V. Schoenfeld, M. Wei, J. W. Mares, A. Scheurer, and R. C. Boutwell; Invited Talk for Wide Bandgap Semiconductor Center of Excellence Seminar Series, Army Research Lab, Adelphi, MD, 2012.

[5] "Cubic Oxide Semiconductors for Deep Ultraviolet Applications (Third Place Award)"; A. Scheurer, R. C. Boutwell, J. W. Mares, and W. V. Schoenfeld; presented at the SHPE National Conference, Cincinnati, OH, 2010.

[6] "Cubic Oxide Semiconductors for Deep Ultraviolet Applications (First Place Award - Engineering)"; A. Scheurer, R. C. Boutwell, J. W. Mares, and W. V. Schoenfeld; presented at the UCF, Showcase of Undergraduate Research Excellence (SURE), Orlando, FL, 2010.

Number of Presentations: 6.00

Non Peer-Reviewed Conference Proceeding publications (other than abstracts):

<u>Received</u>	<u>Paper</u>
-----------------	--------------

TOTAL:

Number of Non Peer-Reviewed Conference Proceeding publications (other than abstracts):

Peer-Reviewed Conference Proceeding publications (other than abstracts):

<u>Received</u>	<u>Paper</u>
-----------------	--------------

TOTAL:

Number of Peer-Reviewed Conference Proceeding publications (other than abstracts):

(d) Manuscripts

Received Paper

TOTAL:

Number of Manuscripts:

Books

Received Book

TOTAL:

Received Book Chapter

TOTAL:

Patents Submitted

[1] Provisional 61/804,299 (Patent Pending) – “Oxide Semiconducting Thin Films for UV Sensors”

Patents Awarded

[1] Patent No. 8,362,476 - "Cubic Semiconductor Alloys for Deep UV Applications".

Awards

Graduate Students

<u>NAME</u>	<u>PERCENT SUPPORTED</u>	Discipline
Jeremy Mares	1.00	
Casey Boutwell	1.00	
Ming Wei	0.15	
FTE Equivalent:	2.15	
Total Number:	3	

Names of Post Doctorates

<u>NAME</u>	<u>PERCENT SUPPORTED</u>
Huiyong Liu	1.00
FTE Equivalent:	1.00
Total Number:	1

Names of Faculty Supported

<u>NAME</u>	<u>PERCENT SUPPORTED</u>	National Academy Member
Winston Schoenfeld	0.30	No
FTE Equivalent:	0.30	
Total Number:	1	

Names of Under Graduate students supported

<u>NAME</u>	<u>PERCENT SUPPORTED</u>	Discipline
Amber Scheurer	1.00	Electrical Engineering
FTE Equivalent:	1.00	
Total Number:	1	

Student Metrics

This section only applies to graduating undergraduates supported by this agreement in this reporting period

The number of undergraduates funded by this agreement who graduated during this period: 1.00

The number of undergraduates funded by this agreement who graduated during this period with a degree in science, mathematics, engineering, or technology fields:..... 1.00

The number of undergraduates funded by your agreement who graduated during this period and will continue to pursue a graduate or Ph.D. degree in science, mathematics, engineering, or technology fields:..... 1.00

Number of graduating undergraduates who achieved a 3.5 GPA to 4.0 (4.0 max scale):..... 1.00

Number of graduating undergraduates funded by a DoD funded Center of Excellence grant for Education, Research and Engineering:..... 0.00

The number of undergraduates funded by your agreement who graduated during this period and intend to work for the Department of Defense 0.00

The number of undergraduates funded by your agreement who graduated during this period and will receive scholarships or fellowships for further studies in science, mathematics, engineering or technology fields:..... 1.00

Names of Personnel receiving masters degrees

<u>NAME</u>	
Casey Boutwell	
Ming Wei	
Jeremy Mares	
Total Number:	3

Names of personnel receiving PhDs

NAME

Jeremy Mares

Casey Boutwell

Ming Wei

Total Number:

3

Names of other research staff

NAME

PERCENT SUPPORTED

FTE Equivalent:

Total Number:

Sub Contractors (DD882)

Inventions (DD882)

Scientific Progress

Scientific progress and accomplishments are listed and discussed in the formal report document.

Technology Transfer

The following Patents resulted from the work:

[1] Patent No. 8,362,476 - "Cubic Semiconductor Alloys for Deep UV Applications".

Deep-UV Emitters and Detectors Based on Lattice-Matched Cubic Oxide Semiconductors (4.2 Optoelectronics)

(Final Report for US Army Research Office)

Period of Performance: 08/01/2012 – 08/31/2014

Contract Number: W911NF-10-1-0159

Author/Affiliation: **Prof. Winston V. Schoenfeld**
CREOL, The College of Optics & Photonics
University of Central Florida
4000 Central Florida Blvd.
Orlando, FL 32826

Report Contents

Report Contents	1
Abstract.....	2
Summary	2
Primary Program Accomplishments	3
MgO Homoepitaxy	5
Extrinsic Doping with Gallium.....	6
Investigation of Oxygen Plasma Conditions	8
Comprehensive Study of Critical ZnMgO Heteroepitaxy Parameters for use as Deep Ultraviolet Sensors.....	16
The Effect of Substrate Temperature and Source Flux	16
The Effect of Oxygen Flow Rate and Radio Frequency Plasma.....	23
Other progress in cubic oxides: NiMgO	32
NiMgO thin films by sol-gel spin coating.....	32
Ozone Source Investigation.....	40
Hardware Preparations.....	40
Growth Efforts with Ozone Source	42
Future work and potential direction	44

Key Words: Oxide Semiconductors, ultra-violet detectors, zinc oxide

Abstract

The program resulted in significant advancement in the growth of rocksalt oxide ternary semiconductors and demonstrated devices. Comprehensive studies were put forth on the interrelation of growth conditions with device performance, resulting in a deeper understanding of the optimized parameters for growth. Efforts led to significant increases in solar-blind detector responsivity (up to 0.1 A/W) with sub-nanoamp dark currents and adjustable band edge. Furthermore, the program resulted in 4 journal publications, 6 conference papers, 1 issued patent, and partial/full support for three graduate students who received their PhD degrees from CREOL.

Summary

This report summarizes the accomplishments toward advancing rocksalt oxide optoelectronics. Although the challenges associated with extrinsic doping forced a redefinition of scope, the resulting work significantly advanced the state and understanding of cubic ZnMgO UV sensors. These results are manifest in the submission of three ZnMgO publications and the filing of a provisional patent.

Primary focus for the initial project was determining the viability of Ga doping of ZnMgO. Initial Ga doping of MgO was not successful, likely due to intrinsic defect compensation as is widely accepted as a challenge for many wide band gap semiconductors. Introduction of Zn increases the potential to realize n-type Ga doping since this moves the conduction band minimum closer to the Fermi pinning level, reducing intrinsic defect compensation effects. Despite the functionality MSM devices we have demonstrated in the past with our cubic oxide films under this program, we learned through a sister ARL cooperative agreement program that our low growth rates (typically under 0.25 $\mu\text{m/hr}$) seem to result in higher impurity incorporation that reduces the lifetime in our films. In response, we put forth an effort to better identify critical growth parameters for our cubic oxide films in an effort to realize higher quality films for improved MSM devices. Critical parameters explored included growth temperature, cation ratio (i.e. source temperature ratio), oxygen flow rate, and oxygen plasma power. Decreased growth temperature produced phase segregated ZnMgO thin films, as did increased Zn cell temperature. Further investigation of growth and cell temperatures identified optimized growth at 450°C with both the Mg and the Zn cell operating at 360°C. The Zn was operated with a small aperture to reduce oxidation. Optical Emission Spectroscopy (OES) identified active species in the plasma; correlating their changing concentrations with changing oxygen flow and plasma power. Increasing oxygen flow rate resulted in smoother films, which also grew faster. The same improvement was identified when increasing the plasma power.

Research has progressed with fervor since the last report filing. Mg/Au ohmic contacts were adhered with Ni for both cubic and phase-separated ZnMgO

films, photodetector fabrication was optimized and repeated across four major growth variables, and the correlation between growth and device performance was explored and explained.

Additionally, an ozone generating source was installed and initial operation explored. Though ozone grown ZnMgO has not yet been demonstrated, initial investigation suggests that high concentration ozone may be produced and injected into the MBE reactor.

Primary Program Accomplishments

1. The program directly supported three Ph.D. graduate students, two fully and one partially, in their dissertation work that resulted in the receipt of their Ph.D. degree.
2. A total of 4 journal publications, 6 conference presentations, and 1 patent resulted from the program, acknowledging ARO's support of the project.
3. MgO buffer layer formation was optimized, resulting in identification of stoichiometric growth conditions in oxygen and Mg-rich atmospheres. MgO epilayer growth at the stoichiometric point was 5x-10x rougher than epilayers grown under oxygen rich conditions. However, oxygen-rich films grew at approximately 25% the growth rate of "stoichiometric" films.
4. Wurtzite/cubic oxide growth "cross-talk" effect was circumvented by insertion of a additional Mg and Zn cells, and staggered rather than concurrent growth campaigns.
5. Over 15 growths were undertaken to realize Ga doping of ZnMgO with various compositions. This included film growth with the Ga cell 350°C hotter than equivalent n-type Ga doping in wurtzite ZnMgO. It was determined that despite the ability to incorporate measurable Ga, it does not result in n-type behavior of ZnMgO. We now believe collaboration with an experience modeling expert is needed in order to identify other likely extrinsic dopants and methods.
6. Ga was discovered to act as a high-quality surfactant for MgO growth, resulting in significant improvements in surface morphology and increasing growth rate by a factor of ~2x.
7. ZnMgO film growth and microstructure evolution were investigated from 300° - 700°C. Zn desorption from the surface was identified with increasing growth temperature. This was correlated with increasing Mg composition with increasing temperatures, and decreasing film thickness.
8. Phase segregation was controlled by varying cation temperature and was identified by X-Ray Diffraction (XRD). Small phase segregated peaks in XRD did not lead to measurable absorption in spectrophotometry, suggesting that slight phase segregation may be tolerable for UV photodetectors.
9. Atomic and molecular active species in the oxygen plasma were identified by OES, and data was collected to correlate their changing emission with

- changing concentration. Changing oxygen source conditions were compared with collected OES data and used to explain changes in epilayer formation.
10. Oxygen source parameters were explored through both varying flow rate into the MBE reactor and varying RF power applied to the oxygen plasma.
 11. Increasing oxygen flow rate resulted in increased Zn incorporation, and can be understood from the difference in Enthalpy of Formation (ΔH) between ZnO and MgO. As ΔH is nearly twice as large for MgO than ZnO, the surface Mg attracts a disproportionate amount of O, which precludes Zn incorporation. As O on the surface is increased, Zn concentration in the film increases correspondingly.
 12. Increasing oxygen flow rate was also correlated with increased concentration of neutral atomic oxygen in the source plasma. This increase also increased Zn incorporation, and was found at high power (high concentration) to result in phase segregation from significant Zn incorporation.
 13. A peak was identified in the device responsivity trend and was correlated with a maximum difference between neutral and ionized atomic oxygen species. This result encourages the use of electrostatic ion traps to filter plasma species impinging on the surface, and maximize the concentration of neutral atomic oxygen.

MgO Homoepitaxy

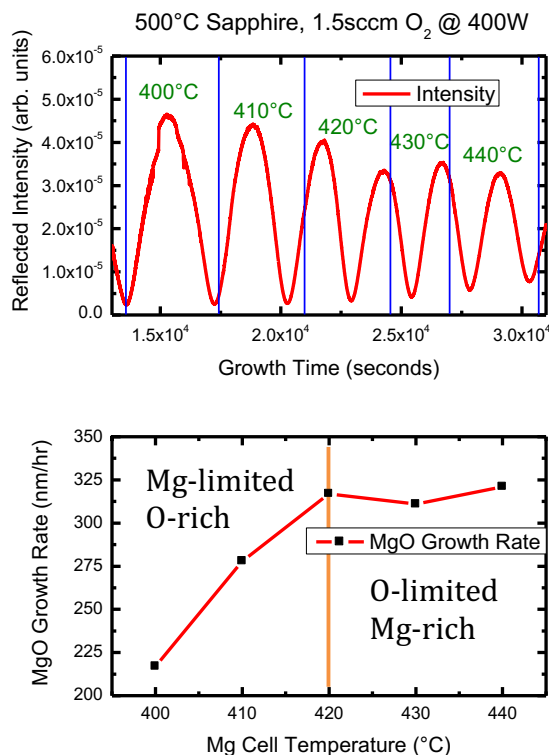


Figure 1: (Top) Laser Reflectometry for MgO on Sapphire Substrates at 1.5sccm, and 500C substrate temperature. (Bottom) Identification of growth limiting regimes as determined by film growth rate at various cell temperatures.

Laser reflectometry analysis was performed at multiple substrate temperatures to understand the change in film composition with varying growth conditions. This information was then translated to MgO homoepitaxial conditions not only to confirm growth rate, but also to investigate the evolution of surface morphology on MgO Substrates.

Figure 2 demonstrates this investigation. These two films were grown at the same substrate condition, but with different Mg cell temperatures. The film on the left was grown near the stoichiometric point (as determined by laser reflectometry) while the film on the right was produced in considerably oxygen rich conditions. This trend is continued through multiple investigations, with O-rich growth consistently leading to smoother film surfaces. However, due to the dramatically reduced cell temperature, growth rate is correspondingly lowered, resulting in increased growth time for similar film thicknesses.

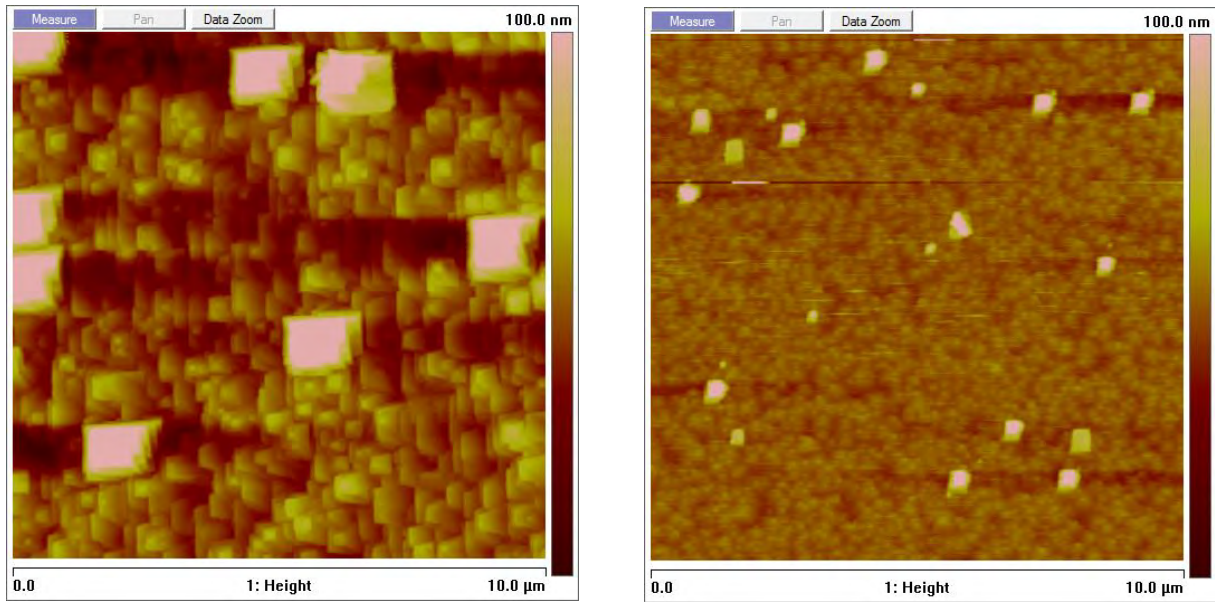


Figure 2: (Left) MgO grown at 425°C shows surface roughness about 9nm, while (right) MgO grown at 330°C under identical oxygen flow shows roughness of 3nm.

Extrinsic Doping with Gallium

Ga was initially considered as a potential dopant in the ZnMgO matrix, as it is well known to n-type dope wurtzite ZnMgO films. Ga incorporation was also investigated in the MgO homoepitaxial films while review was underway, with unexpected results.

Initial doping investigation was performed by Hall characterization on films produced with various Ga cell temperatures. None of these films showed any increase in conductivity, even with changes in characterization temperature. This discouraging result may be to an intrinsic resistance of the wide band gap MgO matrix to accept the necessary dopant atoms to produce measureable carrier increase. This theory is support by the Amphoteric Defect Model, proposed by Walukiewicz in 1989, which suggests that the crystalline matrix will form compensating defects as dopant concentration increases that effectively nullify the impact of increased available carriers. This resistance to doping may be overcome by theoretical modeling or computational investigation of crystalline potentials to identify optimal dopants.

While the resistance to doping is discouraging, an interesting discovery was also made during Ga-rich Mg growth. Figure 3 shows two different MgO films grown under different Ga atmospheres. The left film was produced under Ga overpressure, while the right film was grown with no Ga present.

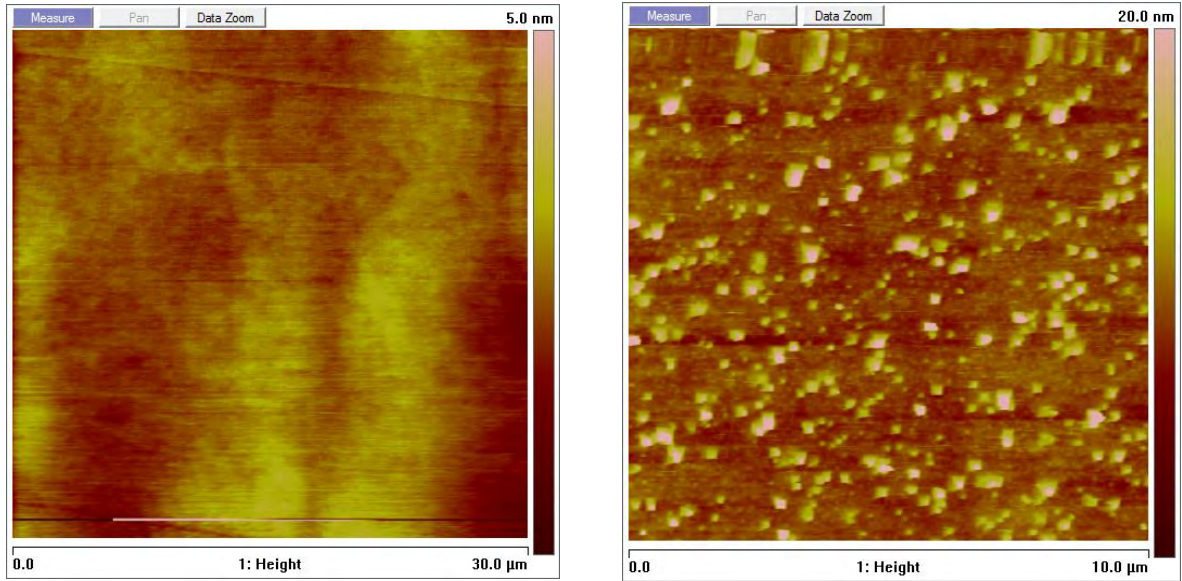


Figure 3: (Left) MgO grown with Ga source at 600C, resulting in roughness of 1.02nm and growth rate of 93nm/hr. (Right) MgO grown with no Ga present resulted in roughness of 2.50nm, and growth rate of 50nm/hr.

Figure 4 expands on the increase in growth rate with increasing Ga temperature. Films grown with higher Ga flux were also smoother than their corresponding non-Ga samples. While this result seems initially to suggest significant Ga incorporation into the MgO film, compositional analysis with RBS shows that this is not the case. The film produced with Ga flux at 650°C, for example, only has approximately 3.2% Ga present in the epilayer.

Here, the Ga appears to act as a surfactant in MgO thin films. Ga surfactant effect is not new in epitaxial growth, but has not before been reported in MgO homoepitaxy. Epitaxial surfactants have been known since the 1980s, and the effect of Ga has a surfactant in epitaxial growth has been known for almost a decade.

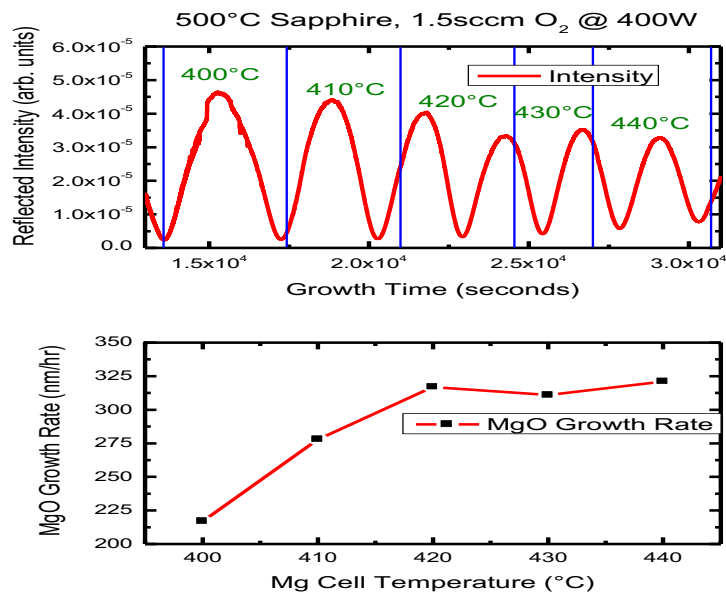


Figure 4: Growth rate increase with MgO grown in Ga-rich conditions.

There are a number of proposed mechanisms for this effect, ranging from lowering of energy barriers on partially completed monolayers to enhanced diffusion through a Ga adlayer which “floats” on the growing film. However, at this point, the specific mechanism for enhanced growth rate and reduced surface roughness of MgO under Ga-rich growth atmosphere is still known.

Investigation of Oxygen Plasma Conditions

In order to understand well the operating conditions of the oxide MBE, the oxygen source was thoroughly characterized and related to properties of the as-grown films. This analysis consisted mainly of Optical Emission Spectroscopy (OES) of the oxygen plasma generated in the source while connected to the UHV system under growth. Oxygen flow rate and applied RF power was varied and correlated with changes in film properties like RMS roughness and growth rate.

This investigation demonstrated unexpected novelty for analysis of oxide MBE, and resulted in original research characterizing low-pressure oxygen plasmas and their impact on film growth dynamics. The work resulted in a publication submitted to the Journal of Alloys and Compounds in June of 2013. Details of the work are below.

Investigation and Impact of Oxygen Plasma Compositions on Cubic ZnMgO Grown by Molecular Beam Epitaxy

Introduction:

ZnMgO thin films attract considerable attention due to the ability to tune optical absorption from the near ultraviolet (NUV) to the deep ultraviolet (DUV) by varying metallic composition [1, 2]. DUV optoelectronics can access the solar blind spectral region, enabling commercial applications ranging from combustion monitors and DUV detectors to UV sterilization equipment. While it is well known that the binaries ZnO and MgO have incompatible crystal structures, Zn-rich ZnMgO (wurtzite B4) and Mg-rich ZnMgO (rocksalt B1) are regularly produced with good crystallinity and smooth surface morphology at different ends of the compositional scale [3, 4]. Adding Mg to the ZnO lattice blueshifts the ternary bandgap, while redshifting is accomplished by adding Zn to MgO [5, 6].

While wurtzite-ZnMgO has received significant attention for its functionality in the NUV spectral range [7, 8], cubic-ZnMgO has recently also begun to receive attention from several research groups. c-ZnMgO possesses many intriguing characteristics worthy of investigation and exploitation by optoelectronic devices. Lattice-matched c-ZnMgO is readily grown on commercially available MgO substrates, and maintains good crystallinity with epilayer roughnesses at the angstrom level [1]. Additionally, c-ZnMgO is inversion symmetric, enabling isotropic conduction of charge carriers and avoiding the polarization fields present in wurtzite phase quantum-confined structures. Devices with internal polarization

fields like those present in wurtzite can suffer from reduced electron-hole overlap similar to the Quantum Confined Stark Effect [9, 10].

While epitaxial ZnMgO thin films are produced by many techniques [11-14], plasma-enhanced Molecular Beam Epitaxy (MBE) offers fine control over process environment by utilizing a Radio-Frequency (RF) oxygen plasma source. Oxygen plasma injection entails a number of unique variables and criteria, including system stability and reproducibility by avoiding oxidation of internal components or reduction of elemental flux through source oxidation [15]. These considerations act as boundary conditions on oxygen flow into the growth reactor and applied power to the injected plasma. Active species in the oxygen plasma must also be considered for their ability to etch and react with substrates and internal machinery, often requiring the use of high voltage deflection plates or electrostatic ion traps at the source aperture to redirect harmful reactive ions and improve net growth rate by reducing film etching [16, 17].

Previous investigations considered the effect of oxygen plasma factors in ZnO, but a thorough study of the impact of oxygen plasma conditions in c-ZnMgO has not been reported [18, 19]. Here we investigate the effect of oxygen flow rate and applied RF power on the growth rate and surface morphology of c-ZnMgO thin films grown on MgO substrates.

Experimental details:

The ZnMgO films were grown in an SVT Associates oxide MBE reactor on 1cm square (100) MgO substrates purchased from MTI Crystal. Praxair Ultra High Purity (99.9999%) oxygen was injected through a mass flow controller at a flow rate of 0.5sccm to 2.5sccm in 0.5sccm steps into the SVT 4.5ALO plasma source. An RF generator operating at 13.56MHz was coupled to the source and supplied powers at 50W increments between 150W and 500W. The ignited plasma was stabilized for 60min before Optical Emission Spectroscopy (OES) was collected by an Ocean Optics Jazz fiber-coupled spectrometer. Each subsequent spectrum was collected after 10 minute stabilization at new operating conditions. Films were grown at substrate temperature of 275°C, with fixed Mg and Zn cell temperatures (345°C and 360°C respectively) for a total of 4 hours of growth per film. The Zn crucible operated with an aperture to reduce source oxidation, while the Mg crucible was operated without an aperture. The plasma source was operated without the use of deflection plates (electrostatic ion traps) which resulted in all species in the plasma impinging on the surface during growth. All substrates were outgassed in a separate ultra-high vacuum chamber for 4 hours at 750°C. The growth chamber base pressure was below 1E-9 Torr and growth pressure ranged from 1E-8 Torr at 0.5 sccm flow rate to 1E-5 Torr at 2.5 sccm.

ZnMgO thin films were investigated with a number of characterization tools. A Veeco Dimension 3100 Atomic Force Microscope (AFM) measured surface morphology while standard contact profilometry measured film thickness and allowed for determination of the film growth rate. A Rigaku D-max X-Ray Diffractometer (XRD) searched for phase segregation in the produced films, while a

Cary 500 UV-Vis Spectrophotometer investigated absorption edge with changing oxygen flow rate and applied RF power.

Spectral peaks were identified from the NIST Atomic Spectra Database [20]. Three active species were detected in the oxygen plasma: neutrally charged atomic oxygen (O I), singly ionized atomic oxygen (O II), and singly ionized molecular oxygen (O_2^+ , the dioxygenyl ion). Excited neutral atomic oxygen (O I) was measured from changes in the 6453Å line, excited singly-ionized atomic oxygen (O II) was identified by the 4367Å line, and changes in excited ionized molecular oxygen (O_2^+) were identified by the vibronic transition at 5248Å. The assumption that changes in emission intensity related directly to changes in plasma composition was applied to correlate the relative concentrations of these active species. This allowed for the determination of relative maxima and minima in the ratio of neutral atomic to ionized atomic oxygen and neutral atomic to ionized molecular oxygen by identifying maxima in the ratio of their emission intensities.

Results and discussion:

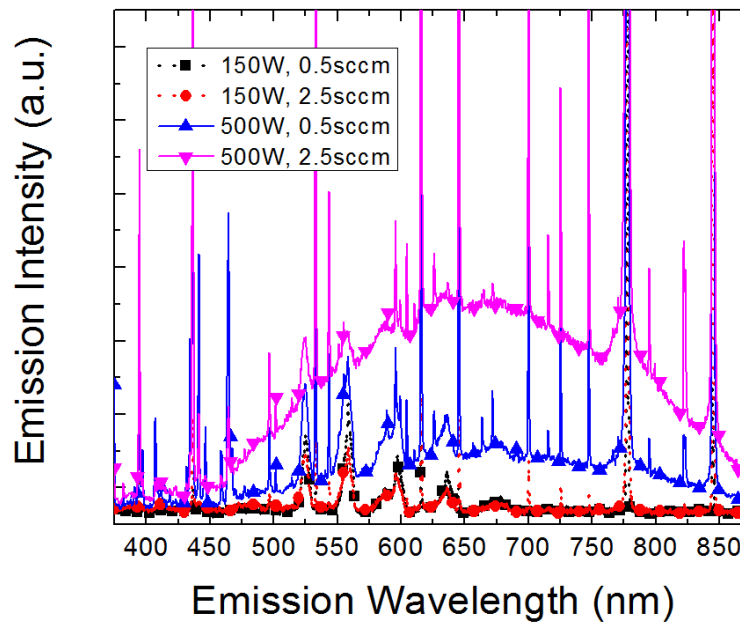


Figure 5: Typical emission spectra of oxygen plasma under extremes of flow and power shows the broad emission of Bremsstrahlung radiation, which is maximized at highest flow and power. The low power curves show strong contribution from molecular oxygen emission, while higher power resulted in strongest emission from oxygen atoms.

Figure 5 shows a typical spectrum collected from optical emission along the axis of the plasma source. The spectrum contains many transitions, but describes only the three active species. The O I spectrum is strongest at the 777 nm and 844 nm unresolved triplets, representing transitions from $3p^5P-3s^5S$ and $3p^3P-3s^3S$ lines respectively. O II emission is brightest from the 436nm peak representing combined emission from transitions between $3p^4P-3s^4P$ and $3d^2D-3p^2D$. O_2^+ emission is evident as broad peaks between 500-650nm representing the first negative O_2^+ system [21]. The spectrometer used did not resolve the fine structure

spin components of these separate transitions, resulting in their appearance as a single emission line. Due to the saturation of the O I spectrum at 777nm and 844nm, the unresolved 615nm triplet for O I corresponding to a $4d^5D-3p^5P$ was chosen to represent changes in O I concentration instead.

Increasing the power and flow rate through the plasma source increased the intensity of the emission lines. At high flow, a broad increase in intensity was observed between 450 nm and 900 nm resulting from Bremsstrahlung radiation emission. This general brightening at high flow covered the emission of a number of spectral lines. At low flow and low power the number of spectral lines was dramatically reduced, and resulted in higher relative intensity of broad molecular emission peaks than atomic lines as seen in Figure 5.

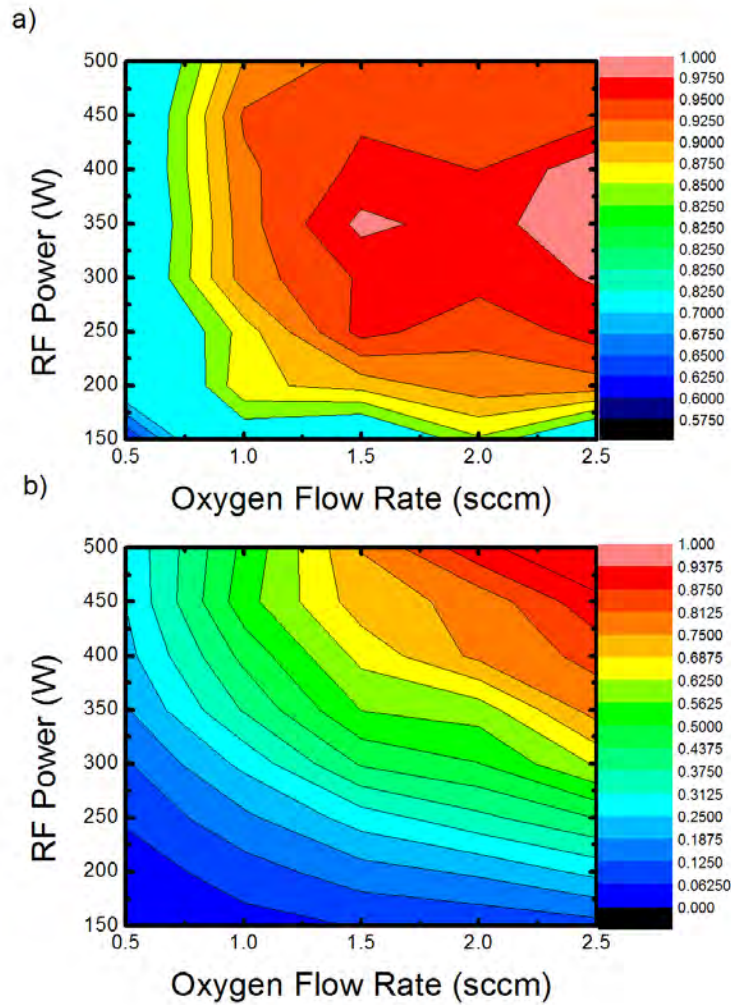


Figure 6: a) The emission intensity ratios of neutral (OI) to ionized (OII) atomic oxygen shows the first relative maximum at 1.5 sccm and 350W. Similar conditions exist at higher flow, but may lead to source oxidation and reduced metal flux. b) Emission intensity ratio of neutral atomic oxygen (OI) to ionized molecular oxygen (O_2^+) showing a monotonic increase with RF power and oxygen flow.

The change in intensity was compared between O I, O II, and O_2^+ to determine relative changes in concentration of active species in the plasma. Figure 6 shows the ratios O I/O II and O I/ O_2^+ as functions of flow rate and RF power. It is interesting to note that the graph shows two maxima to optimize the difference between the neutral atoms and the more reactive atomic ions; at 1.5 sccm and 350W, and at around 2.5 sccm 350W. The first maximum at 1.5sccm may be preferred for growth due to the reduced likelihood of source oxidation at lower oxygen flux.

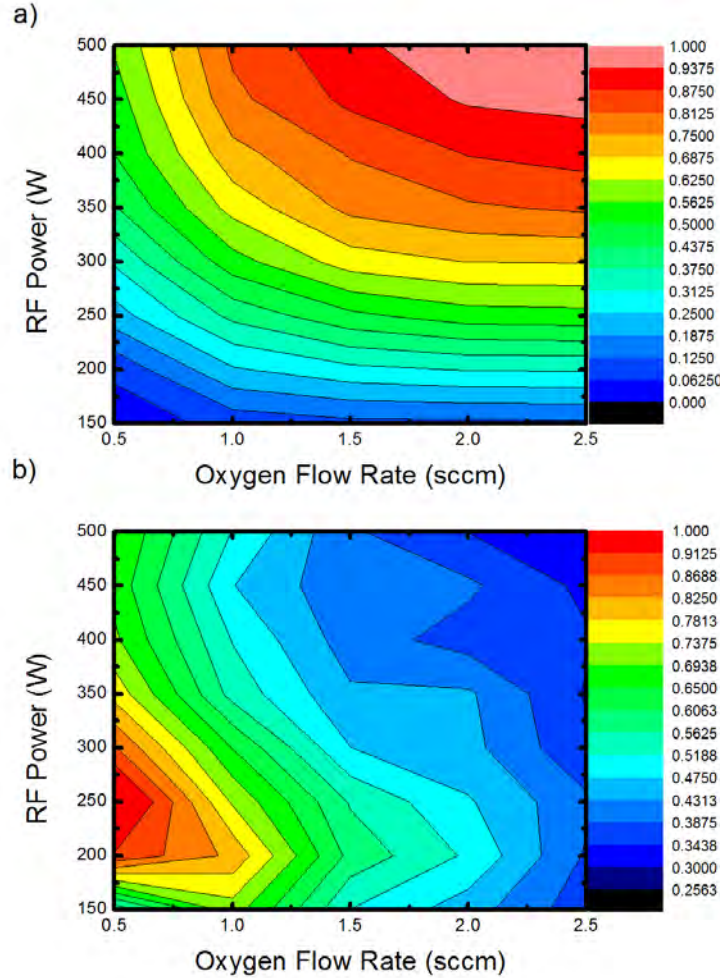


Figure 7: a) Normalized emission intensity of neutral atomic oxygen (OI) showing monotonic increase. b) Normalized emission intensity of ionized molecular oxygen (O_2^+) showing relative maximum at low oxygen flow and low RF power.

To investigate whether this is caused by increasing atomic concentration or decreasing molecular concentration, Figure 6 (b) has been decoupled and is shown in Figure 7. Figure 7a is the normalized absolute intensity of O I measured by OES, while Figure 7b is the normalized absolute intensity of O_2^+ . Figure 7a confirms that as power and oxygen flow rate increase the atomic concentration of the plasma increases monotonically. However, contrary to the case of molecular emission of

nitrogen in GaN growth, where emission intensity increases with power and flow [22], here the molecular emission intensity decreases with increasing power and flow. Figure 7b shows a peak concentration of ionized oxygen molecules at 0.5 sccm and 250W applied RF power. This difference can be explained by their difference in dissociation energies (6.66 eV for O_2^+ and 9.76 eV for N_2) if the molecules were formed from ions/neutrals, as well as a lower ionization potential for O_2 (12.08 eV) than N_2 (15.58 eV) if the molecular ions were formed by ionization. These parameters can explain the existence of neutral N_2 in a larger range of low pressure and low temperature than O_2^+ .

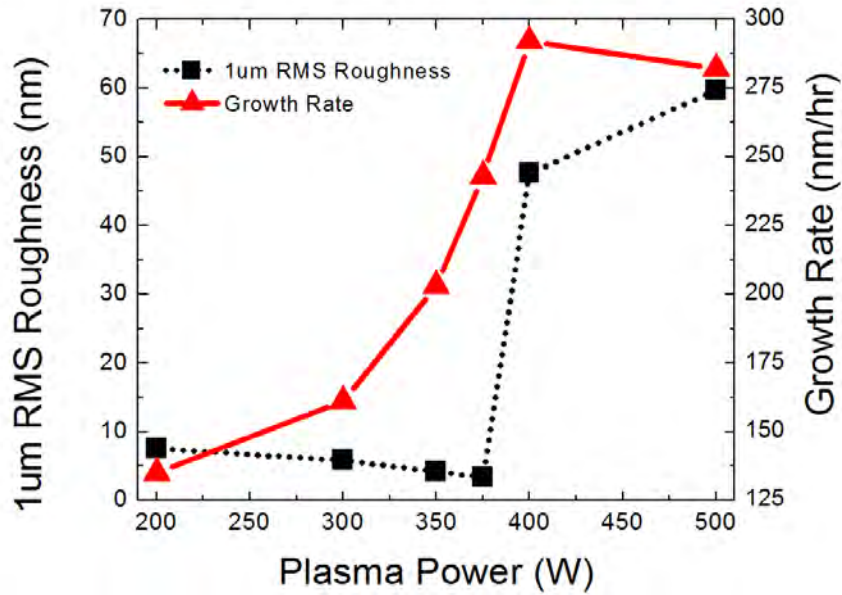


Figure 8: Increasing oxygen plasma power resulted in increased growth rate. 1μm AFM scans showed decreasing roughness until phase segregation began at 400W.

Independently increasing the oxygen flow rate and the applied RF power resulted in increased growth rate and decreased surface roughness of produced ZnMgO films. Increased Zn incorporation was also evident in both cases from optical transmission (not shown). However, in the case of increasing plasma power, it was found that increased Zn incorporation may lead to phase segregation when grown near the miscibility gap. Figure 8 shows the impact of changing RF power on ZnMgO film growth rate and 1μm RMS roughness. As power is increases, the concentration of atomic oxygen rises and allows for greater Zn incorporation, thus increasing the growth rate (solid line). Increased Zn binding results in smoother film surfaces until the incorporation efficiency pushes the film into phase segregation. Segregation occurred at 400W and 500W and resulted in a dramatic increase in film roughness (dotted line).

Increased Zn incorporation with increasing atomic oxygen can be understood by considering the enthalpy of formation (ΔH) for MgO and ZnO. ΔH is nearly twice as high for MgO as it is for ZnO (601 kJ/mol compared to 348 kJ/mol), indicating that at similar surface concentration, MgO formation is energetically favorable. With little available atomic oxygen to bind with in the low flow, low RF power

scenario, Mg accumulates a disproportionate amount of the oxygen on the surface. However, as the atomic oxygen concentration increases (with increasing flow or with increasing RF power), Zn incorporation efficiency is correspondingly increased, allowing for better ZnMgO formation and smoother films.

Conclusions:

Increased oxygen flow rate and RF power were found to result in increased growth rate and reduced roughness. The O I/O₂⁺ ratio increased monotonically with both flow and power, but the O I/O II ratio was found to exhibit a peak at 1.5sccm and 350W RF applied power. This suggests that for smooth ZnMgO films the main damaging reactive species is O₂⁺ not O II, and that it is more important to minimize O₂⁺ than to maximize the difference between O I and O II. Alternatively, a higher concentration of O₂⁺ is beneficial for films with more textured surfaces.

These results show that smooth ZnMgO films with relatively high growth rate may be produced at the high end of the oxygen flow (2.5 sccm) and RF power (500W) investigated. However, as hardware and cation source oxidation is a constant threat, these results indicate that the preferred condition is at 500W, 1.5sccm, where decreased oxygen flow will reduce reactor oxidation and maximize growth campaign duration.

Further investigation with additional *in situ* equipment may enable more direct connections between O I, O II, and O₂⁺ concentrations and their effect on epilayer growth and microstructure evolution. One possible technique to understand these physics more deeply is to operate the oxygen source with deflection plates and a quadrupole mass spectrometer to select active species with a set mass/charge ratio. In this scenario O I, O II, and O₂⁺ could be individually selected and directed at the substrate during growth to determine the empirical impact of oxidation with these three different species.

References

- [1] J.W. Mares, R.C. Boutwell, A. Scheurer, W.V. Schoenfeld, J. Mater. Res., 25 (2010) 1072-1079.
- [2] Y.N. Hou, Z.X. Mei, Z.L. Liu, T.C. Zhang, X.L. Du, Appl. Phys. Lett., 98 (2011).
- [3] L.K. Wang, Z.G. Ju, C.X. Shan, J. Zheng, B.H. Li, Z.Z. Zhang, B. Yao, D.X. Zhao, D.Z. Shen, J.Y. Zhang, J. Cryst. Growth, 312 (2010) 875-877.
- [4] S. Sadofev, S. Blumstengel, J. Cui, J. Puls, S. Rogaschewski, P. Schafer, Y.G. Sadofyev, F. Henneberger, Appl. Phys. Lett., 87 (2005).
- [5] M. Wei, R.C. Boutwell, J.W. Mares, A. Scheurer, W.V. Schoenfeld, Appl. Phys. Lett., 98 (2011).
- [6] W. Yang, S.S. Hullavarad, B. Nagaraj, I. Takeuchi, R.P. Sharma, T. Venkatesan, R.D. Vispute, H. Shen, Appl. Phys. Lett., 82 (2003) 3424-3426.
- [7] T. Gruber, C. Kirchner, R. Kling, F. Reuss, A. Waag, Appl. Phys. Lett., 84 (2004) 5359-5361.
- [8] H. Zhu, C.X. Shan, L.K. Wang, J. Zheng, J.Y. Zhang, B. Yao, D.Z. Shen, J. of Phys. Chem. C, 114 (2010) 7169-7172.

- [9] F. Bernardini, V. Fiorentini, D. Vanderbilt, Phys. Rev. B, 56 (1997) 10024-10027.
- [10] B. Monemar, G. Pozina, Prog. Quantum Electronics, 24 (2000) 239-290.
- [11] W.I. Park, G.C. Yi, H.M. Jang, Appl. Phys. Lett., 79 (2001) 2022-2024.
- [12] J.W. Kim, H.S. Kang, J.H. Kim, S.Y. Lee, J.K. Lee, M. Nastasi, J. Appl. Phys., 100 (2006).
- [13] Y.M. Zhao, J.Y. Zhang, D.Y. Jiang, C.X. Shan, Z.Z. Zhang, B. Yao, D.X. Zhao, D.Z. Shen, ACS Appl. Mater. & Interfaces, 1 (2009) 2428-2430.
- [14] J. Liang, H.Z. Wu, Y.F. Lao, D.J. Qiu, N.B. Chen, T.N. Xu, Chin. Phys. Lett., 21 (2004) 1135-1138.
- [15] Y.S. Kim, N. Bansal, S. Oh, J. Vac. Sci. & Technol. A, 28 (2010) 600-602.
- [16] M. Wei, R.C. Boutwell, G.A. Garrett, K. Goodman, P. Rotella, M. Wraback, W.V. Schoenfeld, J. Alloys Comp., 552 (2013) 127-130.
- [17] T.L. Goodrich, Z. Cai, M.D. Losego, J.P. Maria, K.S. Ziemer, J. Vac. Sci. & Technol. B, 25 (2007) 1033-1038.
- [18] W.C.T. Lee, P. Miller, R.J. Reeves, S.M. Durbin, J. Vac. Sci. & Technol. B, 24 (2006) 1514-1518.
- [19] K. Sakurai, M. Kanehiro, K. Nakahara, T. Tanabe, S. Fujita, S. Fujita, J. Cryst. Growth, 209 (2000) 522-525.
- [20] Y.R. Alexander Kramida, Joseph Reader in, Natl. Inst. Stands. Technol., 2013.
- [21] M. Tuszewski, J.T. Scheuer, J.A. Tobin, J. Vac. Sci. & Technol. A, 13 (1995) 839-842.
- [22] E. Iliopoulos, A. Adikimenakis, E. Dimakis, K. Tsagaraki, G. Konstantinidis, A. Georgakilas, J. of Cryst. Growth, 278 (2005) 426-430.

Comprehensive Study of Critical ZnMgO Heteroepitaxy Parameters for use as Deep Ultraviolet Sensors

The Effect of Substrate Temperature and Source Flux

The impact of major temperature variables in the film grown process was characterized in relation to film properties. Roughness and growth rate were tracked by AFM and standard contact profilometry and correlated with changes in film crystallinity and elemental composition. After complete analysis, identical UV sensors built with interdigitated Ni/Mg/Au Ohmic contacts were fabricated.

This investigation proved very fruitful and enabled a comprehensive comparison between in situ MBE reactor conditions and the ultimate performance of fabricated UV sensors. The work was consolidated and submitted for publication in the journal Applied Surface Science in June of 2013. Details of this work are below:

The Effect of Substrate Temperature and Source Flux on Cubic ZnMgO UV Sensors grown by Plasma-Enhanced Molecular Beam Epitaxy

ZnO and ZnMgO have experienced considerable investigation by the scientific community for application in UV optoelectronics¹⁻³. This is due in part to ZnO's intrinsic radiation hardness compared to silicon and its high excitonic binding energy (60meV)^{4,5}. Additionally, the ZnMgO ternary has demonstrated bandgap tunability from pure ZnO at 3.37eV to pure MgO at 7.8eV. It is well known, however, that the compositional range is not fully miscible and demonstrates a dramatic breakdown in crystalline integrity between approximately 40% and 60% of either cation⁶⁻⁸. This miscibility gap arises as interplay between the crystalline forces of wurtzite-structured ZnO and rocksalt-structured MgO result in phase segregation to Zn-rich wurtzite and Mg-rich cubic regions in the growing thin film⁹. While a large body of research pursues Mg incorporation into the wurtzite ZnO matrix for application in the near-UV (NUV, 300-400nm), relatively little work has investigated Zn incorporation into cubic MgO for deep-UV/solar-blind applications (DUV, 220-280nm).

ZnMgO has been grown by Metal Organic Chemical Vapor Deposition, Pulsed Laser Deposition, and Molecular Beam Epitaxy (MBE) among others and is often reported grown on silicon or sapphire substrates¹⁰⁻¹³. While promising devices have been fabricated and reported in the past, there has not been a detailed review of the impact of growth temperature or cation flux ratio on film growth and optoelectronic device performance. Understanding the impact of these two critical parameters will enable device design with enhanced performance and a better understanding of the tunability in growth and fabrication.

This letter reports on the MBE growth of cubic ZnMgO on commercially available MgO substrates. Interdigitated Metal-Semiconductor-Metal (MSM)

photoconductors were fabricated and spectrally analyzed to determine the impact of growth conditions on the final UV sensor responsivity.

An SVT Associates oxide MBE reactor under ultra-high vacuum ($<10^{-10}$ Torr) housed standard Knudsen cells with 6N Zn and 3N8 Mg provided by Alfa Aesar. In this report, the 40cc Zn crucible was operated with a circular aperture (~ 0.1 inches) to reduce source oxidation and the 40cc Mg crucible was operated without an aperture. Ultra high purity (6N) oxygen was injected into the growth chamber through an inductively-coupled radio-frequency (RF) plasma generator operating at 13.56MHz and directed with the metal flux onto a 1cm^2 (100) MgO substrate supplied by MTI Inc. Four substrate temperatures were investigated (400°C, 450°C, 475°C, and 500°C) with identical Knudsen cell fluxes (Zn at 360°C and Mg at 350°C), fixed oxygen flow rate (1.5sccm), and fixed applied plasma power (400W). Six films were also produced with different cation flux ratios at low fixed substrate temperature (LT, 275°C) to investigate the shift in responsivity with changing film composition. This resulted in pure ZnO on MgO, Homoepitaxial MgO, and four films between with Mg cell temperature of 325°C, 340°C, 350°C, and 360°C with a fixed Zn cell temperature of 360°C.

Deposited films were investigated by X-Ray Diffraction (XRD) for phase segregation by a Rigaku D-Max X-Ray Diffractometer as well as by a Veeco Dimension 3100 Atomic Force Microscope (AFM) for the evolution of surface roughness. Rutherford Back Scattering (RBS) determined film composition as a function of substrate temperature, while a Cary 500 UV-Vis-IR spectrophotometer investigated film transmission. Average hourly growth rate was calculated by standard contact profilometry.

Interdigitated MSM contacts were formed with a BOC-Edwards 306 (FL400) thermal evaporator using a Mg/Au contact with $200\text{\AA}/800\text{\AA}$ thickness deposited upon a 30\AA Ni adhesion layer without annealing. The Ohmic Mg/Au contact was chosen to match the low work-function of Mg with the low electron affinity of MgO, which was expected to be close to the work function of the cubic ternary films due to the cubic structure and lower Zn incorporation. Two-point probe IV characterization of the fabricated optoelectronic devices was accomplished with a Keithley 2400 sourcemeter. The devices were exposed by a monochromator to light from a Xe lamp operating at 500W at 5nm intervals while current was measured through the device. Spectral responsivity was calculated by dividing photo-generated current by the optical power spectrum of the lamp. A UV-visible rejection ratio (RR) was also calculated from Responsivity \otimes by $R_{\text{peak}}/R_{400\text{nm}}$.

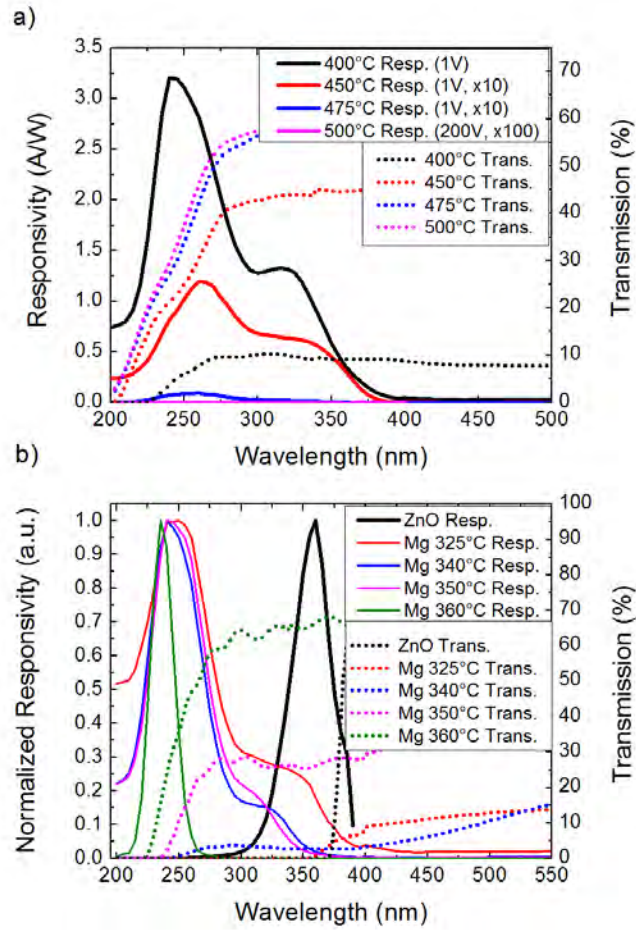


Figure 9: a) Increasing substrate temperature shows blue-shifting of the absorption edge in transmission (dotted lines). Substrate temperature increase also reduced NUV responsivity (solid lines) as Zn incorporation was correspondingly reduced. b) Increasing Mg flux also blue-shifted absorption edge (dotted lines) as phase segregation was suppressed. This eventually resulted in a purely solar-blind responsivity (solid lines).

The effect on responsivity and transmission is shown in Figures 9a and 9b for changing substrate temperature and Mg flux. In Figure 9a it is clear that photoresponse (solid lines) from the sample grown at 400°C shows two overlapping peaks centered at 317nm and 242nm. This reveals the formation of a Zn-rich wurtzite ZnMgO zone and a Mg-rich cubic ZnMgO zone respectively. Increasing the growth temperature to 450°C made these features less distinct and led to DUV dominance by 475°C with a peak near 256nm and no independent wurtzite-rich feature. Combining this trend with a correlated decrease in peak responsivity suggests increasing growth temperature increased relative Mg concentration and reduced photoresponse intensity. The optical transmission data, shown in Figure 9a as dotted lines, supports this analysis. Transmission from the sample grown at 400°C showed two absorption shoulders (one in the NUV and one in the DUV), indicating phase segregation, with the corresponding roughness (53nm per 1 μ m²) of the sample dramatically reducing the amount of transmitted light. Increasing the

substrate temperature reduced phase segregation and blue-shifted the absorption shoulder.

A similar trend was observed for increasing Mg flux on samples grown at LT, shown in Figure 9b. Initially, a low ratio of Mg/Zn evaporation (as determined by relative cell flux) resulted in a similar two-shoulder absorption seen in the substrate temperature investigation. At a low cation ratio, spectrophotometry (dotted lines) indicated a reduction in transmission, suggesting phase segregation later confirmed by XRD (not shown here). This is particularly evident for the sample grown with the lowest Mg flux (Mg 325°C). At this low flux ratio, absorption by Zn-rich wurtzite crystallites collected virtually all incident radiation by 358nm. While this is very near the responsivity peak of the ZnO/MgO film (360nm), and seems to suggest poor Mg incorporation, responsivity from this Mg 325 film actually peaked at 250nm. However, despite absorption peaked in the DUV, a significant photocurrent was generated by a second shoulder in the NUV, yielding a relatively poor RR from poor crystal quality. Further increasing the Mg cell flux reduced the distinct NUV shoulder. However, wurtzite diffracted peaks were visible by XRD in all films until the Mg cell temperature was raised to 360°C (a cell temperature ratio of 1:1 in this experimental setup). For this sample no NUV shoulder was visible in responsivity, XRD identified only cubic peaks, and transmission showed abrupt absorption at 230nm (5.4eV). This film showed the highest RR and clear DUV responsivity peaked at 236nm.

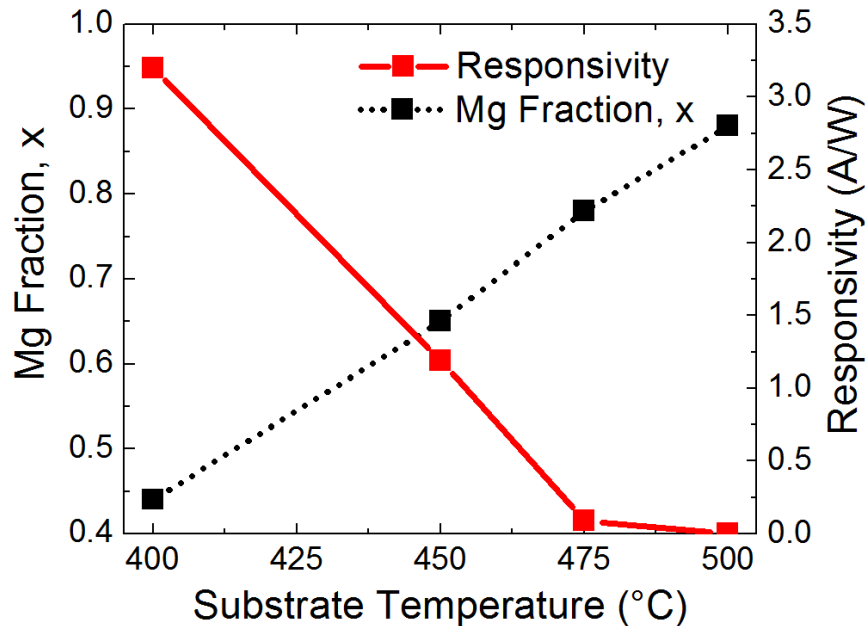


Figure 10: Increasing substrate temperature resulted in increased Mg concentration (x) in the film. This increase in Mg concentration was correlated with a decrease in responsivity.

As indicated above, XRD analysis revealed that at a substrate temperature of 400°C the ZnMgO film segregated into wurtzite and cubic rich regions producing relatively quick three dimensional growth and a correspondingly rough surface. Figure 2 summarizes the change in responsivity with the change in film composition versus substrate temperature. Interestingly, analysis by RBS also showed that even

while Zn and oxygen conditions remained unchanged, Mg concentration in the film increased with increasing substrate temperature. As growth rate slowed with increasing growth temperature, this suggests that Zn may be desorbing from the substrate surface before it can stably bond into the crystal. XRD showed strong wurtzite peaks relative to the cubic substrate at 400°C and 450°C, with weak wurtzite peaks at 475°C and no phase segregation at a growth temperature of 500°C. The Zn cell flux was held at a constant 360°C for these four films.

One possible reason for the observed behavior is that the enthalpy of formation (ΔH) for MgO (601 kJ/mol) is significantly higher than that of ZnO (348 kJ/mol)^{14,15}. This suggests that MgO formation may be energetically favorable to ZnO formation with increasing growth temperature. The growth may be further influenced by the availability of the MgO substrate matrix used for film nucleation.

Figure 10 also reveals that increasing substrate temperature (and thereby increasing Mg concentration) corresponds to decreasing responsivity from fabricated devices, as first suggested in Figure 9b. It is important to note that while the film grown at 400°C (with strong wurtzite peaks visible in XRD) revealed a broad visible blind response corresponding to the phase segregated transmission band edge, the film grown at 500°C showed no measureable photocurrent down to 200nm.

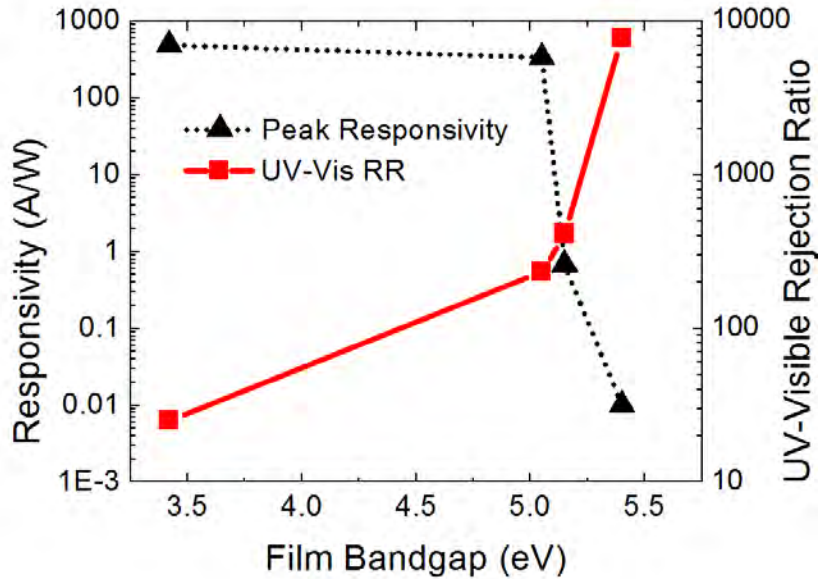


Figure 11: Increasing Mg cell flux resulted in a dramatic decrease in peak responsivity intensity (dotted line). The decrease in responsivity, however, was observed with a corresponding increase in RR.

Increasing the Mg cell flux also resulted in decreased responsivity, following the trend identified with substrate temperature and Mg concentration. This is shown in Figure 11, where the bandgap for each film was calculated and is compared with the trend observed for responsivity intensity and RR. The effective cell temperature range was found to be very narrow for controlling the resulting composition of the film. Changing the cell temperature by twenty five degrees resulted in a precipitous drop in responsivity (from A/W to mA/W) as Mg

incorporation displaced that of Zn on the film surface (Figure 10), rapidly blueshifting the band edge (as shown in Figure 9b). The films produced with low Mg flux (at 3.4eV and 5.1eV) showed photoresponse measured at 100s of Amps per Watt, while the film grown with equal Mg and Zn cell temperatures (5.4eV) showed approximately 10mA/W.

However, a corresponding improvement in RR was noticed with increasing band gap as well as a reduction in phase segregation. XRD analysis revealed wurtzite peaks in films with bandgaps of 3.42eV, 5.1eV, and 5.2eV, which corresponded to broad visible blind photoresponse. The film grown with a bandgap at 5.4eV, on the other hand, showed narrow solar-blind photoresponse centered at 236nm and a rejection ratio three orders-of-magnitude better than films with low Mg incorporation.

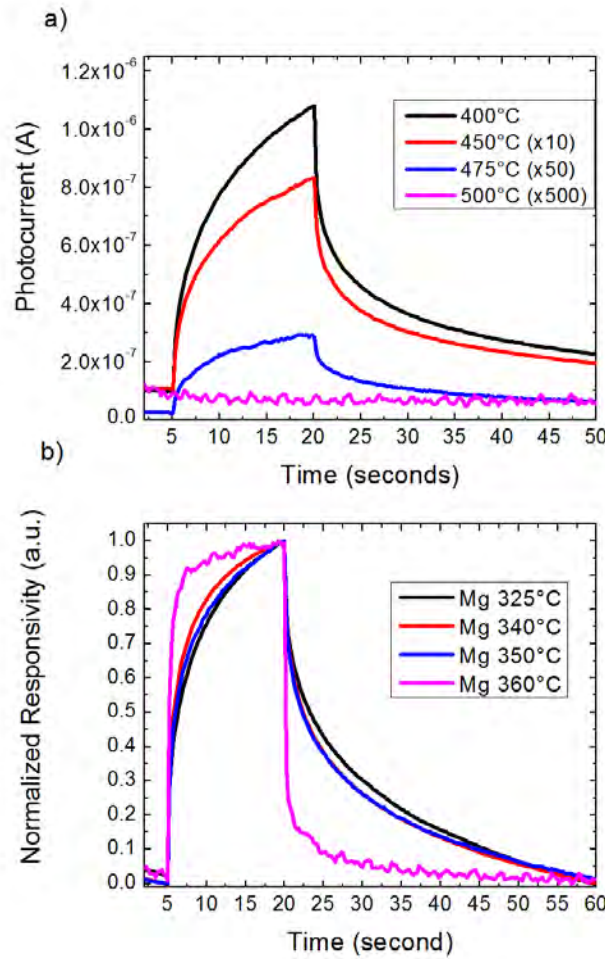


Figure 12: a) Increasing substrate temperature reduced photocurrent but showed no impact on persistent photoconductivity. b) The impact on persistent photoconductivity when transitioning from mixed to single phase films is evident with normalized axis.

Another important realization is the effect of phase segregation on persistent photoconductivity and device response time, as shown in Figure 12a and 12b. This effect, which is commonly related to defects or poor crystal quality, would be

expected in phase segregation^{16,17}. This effect was seen while investigating substrate temperature (shown in Figure 12a) and while investigating Mg flux (Figure 12b). While phase-segregated films did demonstrate higher (though broader) responsivity, they also demonstrated a significant decay time after shuttering the monochrometer. This decay time lasted for tens of seconds and was unaffected by increasing substrate temperature or Mg concentration until phase segregation yielded to cubic single-crystal films. This transition occurred with greatest Mg incorporation, at Mg 360°C in Figure 12b, where device rise and fall times were noticeably reduced once the single-crystal transition was accomplished. Reducing persistent photoconductivity suggests a reduction in crystalline defects trapping photo-induced carriers in long lived states.

Tuning growth temperature and Mg concentration in cubic ZnMgO films plays a very important role in targeting DUV/solar-blind sensor properties. Phase-segregated films can produce high visible-blind photoresponse, though suffered noticeably reduced RR. Single-crystal cubic detectors demonstrate reduced persistent photoconductivity and improved RR, though much weaker UV photoresponse. Effective detectors could also be fabricated with these films through the use of amplifying electrical circuits.

References

- ¹ Y. N. Hou, Z. X. Mei, Z. L. Liu, T. C. Zhang, and X. L. Du, *Appl. Phys. Lett.* **98** (2011).
- ² J. W. Mares, R. C. Boutwell, A. Scheurer, and W. V. Schoenfeld, *J. Mater. Res.* **25**, 1072 (2010).
- ³ M. Wei, R. C. Boutwell, G. A. Garrett, K. Goodman, P. Rotella, M. Wraback, and W. V. Schoenfeld, *J. Alloys Comp.* **552**, 127 (2013).
- ⁴ F. D. Aurret, S. A. Goodman, M. Hayes, M. J. Legodi, H. A. van Laarhoven, and D. C. Look, *Appl. Phys. Lett.* **79**, 3074 (2001).
- ⁵ S. H. Park, *J. Korean Phys. Soc.* **51**, 1404 (2007).
- ⁶ W. Yang, S. S. Hullavarad, B. Nagaraj, I. Takeuchi, R. P. Sharma, T. Venkatesan, R. D. Vispute, and H. Shen, *Appl. Phys. Lett.* **82**, 3424 (2003).
- ⁷ Dinesh Thapa, Jesse Huso, Hui Che, Michelle Huso, John L. Morrison, Diana Gutierrez, M. Grant Norton, and Leah Bergman, *Appl. Phys. Lett.* **102** (2013).
- ⁸ A. Singh, A. Vij, D. Kumar, P. K. Khanna, M. Kumar, S. Gautam, and K. H. Chae, *Semicond. Sci. Technol.* **28** (2013).
- ⁹ M. Wei, R. C. Boutwell, J. W. Mares, A. Scheurer, and W. V. Schoenfeld, *Appl. Phys. Lett.* **98** (2011).
- ¹⁰ J. Liang, H. Z. Wu, Y. F. Lao, D. J. Qiu, N. B. Chen, and T. N. Xu, *Chin. Phys. Lett.* **21**, 1135 (2004).
- ¹¹ W. I. Park, G. C. Yi, and H. M. Jang, *Appl. Phys. Lett.* **79**, 2022 (2001).
- ¹² Y. M. Zhao, J. Y. Zhang, D. Y. Jiang, C. X. Shan, Z. Z. Zhang, B. Yao, D. X. Zhao, and D. Z. Shen, *ACS Appl. Mater. & Interfaces* **1**, 2428 (2009).
- ¹³ L. K. Wang, Z. G. Ju, C. X. Shan, J. Zheng, B. H. Li, Z. Z. Zhang, B. Yao, D. X. Zhao, D. Z. Shen, and J. Y. Zhang, *J. Cryst. Growth* **312**, 875 (2010).

- 14 David R. Lide, (CRC Press, Boca Raton, FL, 2005).
- 15 William L Masterson and Cecile N. Hurley, *Chemistry: Principles and Reactions*, Fifth ed. (Thomson Brooks/Cole, Belmont, Ca, 2004).
- 16 X. Z. Dang, C. D. Wang, E. T. Yu, K. S. Boutros, and J. M. Redwing, *Appl. Phys. Lett.* **72**, 2745 (1998).
- 17 S. Hullavarad, N. Hullavarad, D. Look, and B. Claflin, *Nanoscale Res. Lett.* **4**, 1421 (2009).

The Effect of Oxygen Flow Rate and Radio Frequency Plasma

After understanding the correlation between growth temperature and source flux with UV sensor performance, we endeavored to explore the relationship between oxygen growth conditions and the fabricated UV sensors. To investigate this relationship we varied oxygen flow rate and applied RF power to the plasma and correlated changes in material properties with the final fabricated detectors.

This work was also very enlightening and resulted in submitted publication to Applied Physics Letters in June of 2013. Details of the investigation are below:

The Effect of Oxygen Flow Rate and Radio Frequency Plasma Power on Cubic ZnMgO Ultraviolet Sensors grown by Plasma-Enhanced Molecular Beam Epitaxy

Introduction

ZnO and $\text{Zn}_{1-x}\text{Mg}_x\text{O}$ have attracted much attention due to their oft-cited high excitonic binding energy (60meV) and ability to tune optical absorption from the near UV (NUV) through the deep UV (DUV)¹⁻⁵. This tuning is accomplished by alloying ZnO (E_g - 3.37eV) with MgO (E_g - 7.8eV) and allows for the formation of tunable optoelectronic detectors within that range. It is also well known, however, that the compositional range between ZnO and MgO is interrupted by a crystalline miscibility gap where the wurtzite crystal structure of ZnO is structurally incompatible with the cubic rocksalt structure of MgO^{6,7}. This miscibility gap generally occurs between $x = 0.4$ to 0.6 with some variation between the methods of growth employed⁸.

While a large amount of investigation has been performed on wurtzite $\text{Zn}_{1-x}\text{Mg}_x\text{O}$, significantly less exploration has occurred for its cubic sibling. Cubic $\text{Zn}_{1-x}\text{Mg}_x\text{O}$ films produced by a variety of methods have been investigated to understand bandgap evolution and structural stability, but little literature has thoroughly investigated the performance of fabricated optoelectronic devices. In this article, cubic $\text{Zn}_{1-x}\text{Mg}_x\text{O}$ thin films were produced by Plasma-Enhanced Molecular Beam Epitaxy (PE-MBE). Three series of films were grown; two with varying Radio-Frequency (RF) power applied to the oxygen plasma and one with varying oxygen flow rate into the MBE reactor. Interdigitated electrical contacts were fabricated

with Ni/Mg/Au and the impact of oxygen growth conditions on device responsivity was investigated.

Experimental Methods

An SVT Associates oxide MBE was used with thermal Knudsen cells for metal sources and an RF generator was employed for the creation of oxygen plasma. Commercially available (100) MgO substrates were backside coated with 1 μ m of titanium for thermal homogeneity of the film during growth. Zinc (6N), magnesium (3N8), and high purity oxygen (6N) were injected into the reactor at a fixed low substrate temperature of 275°C. Five flow rates were chosen for investigation ranging from 0.5sccm to 2.5sccm at a fixed RF power (350W). Afterwards, six RF powers were applied to the plasma at fixed oxygen flow rate (1.5sccm) and ranged from 200W to 500W. The produced films were investigated by optical transmission with a Cary 500 UV-Vis Spectrophotometer to determine changes in the absorption edge. A Rigaku D-max X-Ray Diffractometer (XRD) utilizing the Cu k-alpha line was used to determine crystalline composition and to identify phase segregation. In-situ laser reflectometry determined average hourly growth rate, which was confirmed with standard contact profilometry.

Ni/Mg/Au (30Å/200Å/800Å) Metal-Semiconductor-Metal (MSM) contacts were deposited by thermal evaporation in a BOC Edwards 306 (FL400) metalizer. Contact geometry was 500 μ m square with 10 μ m finger width and 10 μ m spacing. Fabricated devices were illuminated with a Xe lamp (500W) and a Newport 74125 monochromator collected with a sapphire lens. Spectral responsivity was calculated by dividing the measured photocurrent by incident optical power as $(I_{\text{light}} - I_{\text{dark}})/P_{\text{optical}}$ at each wavelength.

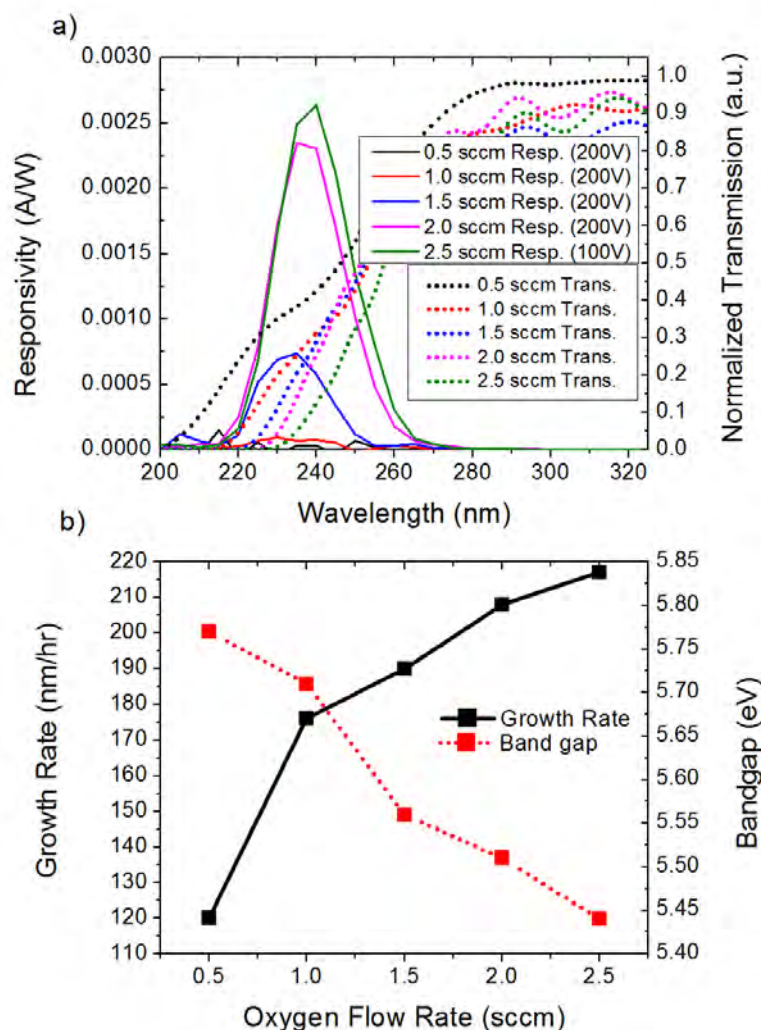


Figure 13: a) Increasing flow rate Increased Zn incorporation, as seen in transmission data (dotted lines). This increase is also correlated with an increase in device responsivity (solid lines). b) Decreasing bandgap (dotted line) is explained by increased Zn incorporation. Increased oxygen flow increases the availability of oxygen atoms on the substrate surface, further increasing growth rate contributed by Zn (solid line).

Increasing the oxygen flow rate into the reactor produced a noticeable change in the growth and composition of the film, as shown in Figure 13. Relatively little zinc incorporation was detected by optical transmission at the low flow rate of 0.5sccm. However, increasing the oxygen flow rate resulted in greater Zn incorporation in the film, redshifting the absorption edge, as shown as dashed lines in Figure 13a. Increasing oxygen flow rate also had a noticeable impact on the fabricated device responsivity, also shown as solid lines in Figure 13a. While no photoresponse was detected at the low end of the flow rate investigated, the responsivity gradually increased with increasing flow. It is important to note that most of the devices were tested at 200V to collect the most distinct signal. However, none of the devices tested which were grown at 2.5sccm survived testing at 200V,

and were instead tested at 100V to avoid destruction of the contact. Similar 100V scans on films produced with 1.5sccm and 2.0sccm showed approximately half the responsivity intensity as testing at 200V, suggesting that the responsivity for the 2.5sccm sample may be twice as intense.

An increase in Zn incorporation with increasing oxygen flow rate is understood by comparing the ZnO and MgO enthalpies of formation, ΔH . With a ΔH of 601kJ/mol and 348kJ/mol for MgO and ZnO respectively, MgO's formation is much more energetically favorable than that of ZnO^{9,10}. This results in a scenario where mobile Mg on the substrate surface is bonding with much of the available O, leaving the Zn adatoms without suitable bonding sites, i.e. when the surface is Mg-rich and O-poor Zn incorporation efficiency is reduced. As the surface concentration of oxygen increases, the Mg adatoms are satiated and the Zn adatoms are able to bond. The increase in oxygen flow rate also increases the growth rate, seen in Figure 13b. This is expected from the higher arrival rate of oxygen species to the surface as well as the improved incorporation of Zn in the $\text{Zn}_{1-x}\text{Mg}_x\text{O}$ matrix. Figure 13b also shows the red-shifting in bandgap as increased Zn incorporation follows from increasing growth rate.

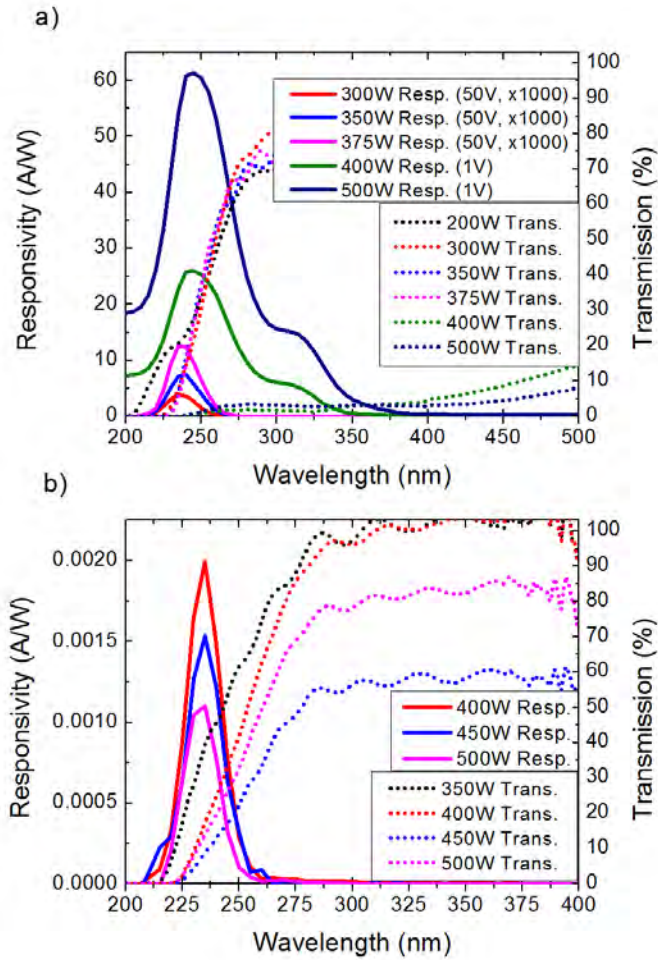


Figure 14: a) In the first plasma series, S1, increasing plasma power eventually led to phase segregation and a dramatic increase in responsivity in the NUV. b) In the second plasma series, S2, increasing the plasma power with a greater starting concentration of Mg yielded reduced responsivity intensity and did not result in phase segregation.

The effect of changing RF power applied to the oxygen plasma is shown in Figure 14. Two different growth series were used to investigate the cubic Zn_{1-x}Mg_xO behavior in this range. The first of these series, shown in Figure 14a, was grown with an absorption edge near the miscibility gap (measured at ~230nm, 5.4eV). The second plasma power investigation series, Figure 14b, was grown with an absorption edge deeper in the UV (measured at ~220nm, 5.6eV). In the near-gap case, increasing the RF power applied increased the magnitude of measured responsivity. However, while the response was solar-blind at 300W, 350W, and 375W, phase segregation occurred at 400W and 500W. This segregation is understood from crystalline interplay on the surface under growth as competition between wurtzite and cubic rocksalt phases¹¹. This expanded the response region into the NUV and producing sensors that were visible blind. No response was measured for the film produced at 200W, even with 200V applied. Visible blind (phase segregated) sensors showed strong photoresponse with only 1V applied, as

compared to the 50V applied to solar-blind sensors. Phase segregation was confirmed by wurtzite peaks in XRD, two absorption edges in optical transmission, and a substantial NUV shoulder in the responsivity. While the phase segregated samples did show a broader visible-blind response, the intensity of their response was over three orders of magnitude greater than the single-crystal DUV sensors. A slight increase in Zn incorporation is also seen in Figure 14a between the 200W transmission data when compared to the absorption edge of the rest.

In the second power series, all devices were tested at 200V for greatest signal intensity. Increasing power again resulted in a slight increase in Zn incorporation, evident in transmission data in Figure 14b. Responsivity, also shown in Figure 14b, was not detected from the 350W sample, but rather peaked at 400W and is steadily reduced with increasing power. This behavior is best understood in Figure 15.

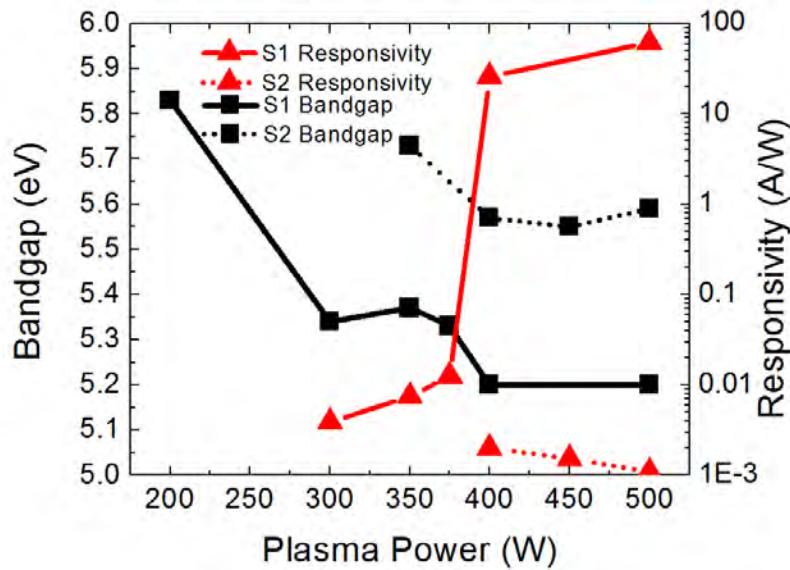


Figure 15: Increasing plasma power increases Zn incorporation and lowers the bandgap (square points) for both S1 and S2. Responsivity (triangular points) of single crystal films peaked about 375W. This corresponds with a maximum of the ratio OI/OII in the oxygen plasma composition.

Figure 15 shows the relationship between plasma power, film bandgap, and device responsivity. It appears that increasing plasma power has a very slight effect of increasing Zn incorporation, thereby red-shifting the bandgap (squares). If the bandgap of the film is near the point of crystalline immiscibility, then increasing plasma power was found to increase Zn incorporation to the point of phase segregation, the case of 400W and 500W in Plasma Series 1. Phase segregation is avoided, however, if the bandgap is further from the immiscibility edge. As RF power to the plasma is increased, the concentration of atomic oxygen increases. This increase in available atomic oxygen enhances the inclusion of Zn in the growing film, resulting in a slight narrowing of the bandgap.

Figure 15 also shows the responsivity as a function of plasma power for both Series 1 (S1) and Series 2 (S2). This behavior seems more erratic, but is rooted in the same physics as the change in Zn inclusion. The major constituents in the oxygen plasma are continually evolving as RF power increases. These active

constituents include neutrally charged atomic oxygen (OI), singly ionized atomic oxygen (OII), and singly ionized molecular oxygen (O_2^+ , the dioxygenyl ion). Emission spectra collected from the oxygen plasma indicate that there is a maximum in the ratio of neutral to ionized atomic oxygen (OI/OII) around 350W, which decreases gradually in both directions. Contrary to nitrogen plasmas, the oxygen plasma source produces less molecular emission at increased power and flow¹². The responsivity shown in Figure 15 (triangular points) suggests a relationship between maximizing neutral atomic oxygen and increasing photoresponse intensity. Response from S2 is of lower intensity because the bandgap for these films is wider, similar to the device performance seen in Figure 13a. S1 devices grown at 400W and 500W led to phase segregation due to Zn incorporation pushing the composition over the miscibility edge. Transition into the miscibility gap dramatically increased the responsivity magnitude but passed responsivity from solar-blind to visible-blind performance.

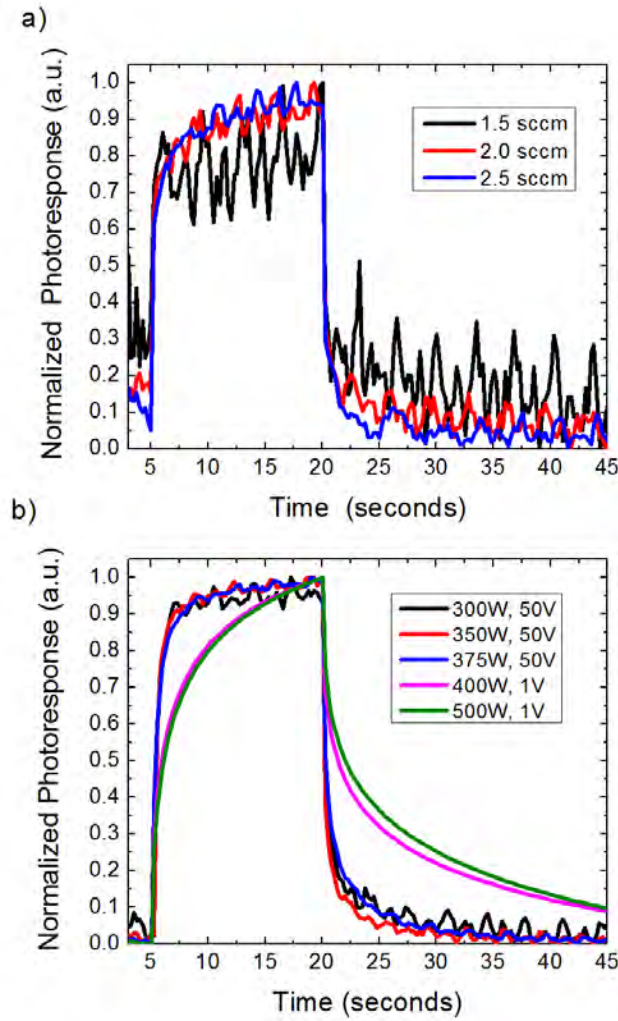


Figure 16: a) Persistent photoconductivity was not found to vary considerably with increasing oxygen flow rate. b) Phase segregated samples displayed considerably longer carrier lifetimes than single-crystal films. Neither RF power study indicated a correlation with plasma power.

The devices produced also exhibited a persistent photoconductivity, as shown in Figure 16. This effect was most pronounced for phase segregated films created at high RF power as shown in Figure 16b, likely due to the increased concentration of deep defects^{13,14}. The effect is also evident to a lesser degree in non-phase-segregated sensors. The concentration of responsible defect(s) does not change relative to responsivity intensity, suggesting that oxygen flow rate and RF power do not affect the charging/discharging. This is evident because increasing oxygen flow rate and plasma power appeared to affect responsivity and charging/discharging times equally. The unaffected behavior is seen in Figures 16a and 16b where responsivity has been normalized to show no significant change in charging/discharging when varying growth conditions.

Conclusion

Increasing oxygen flow rate and RF plasma power both lead to increased Zn incorporation and red-shifting of the bandgap. This red-shifting is caused by the increase in available atomic oxygen on the substrate surface when increasing either the oxygen flow rate or increasing RF power. These results suggest that the condition for the most intense device responsivity will likely be at a high oxygen flow rate with applied RF power between 375W and 400W and an absorption edge near to the miscibility gap. Phase-segregated $\text{Zn}_{1-x}\text{Mg}_x\text{O}$ showed promise for visible-blind detectors and may be explored further by exploiting segregation caused by these two oxygen growth conditions.

References

- 1 Y. N. Hou, Z. X. Mei, Z. L. Liu, T. C. Zhang, and X. L. Du, Appl. Phys. Lett. **98** (2011).
- 2 F. D. Aurret, S. A. Goodman, M. Hayes, M. J. Legodi, H. A. van Laarhoven, and D. C. Look, Appl. Phys. Lett. **79**, 3074 (2001).
- 3 J. W. Mares, R. C. Boutwell, A. Scheurer, and W. V. Schoenfeld, J. Mater. Res. **25**, 1072 (2010).
- 4 S. H. Park, J. Korean Phys. Soc. **51**, 1404 (2007).
- 5 M. Wei, R. C. Boutwell, G. A. Garrett, K. Goodman, P. Rotella, M. Wraback, and W. V. Schoenfeld, J. Alloys Comp. **552**, 127 (2013).
- 6 A. Singh, A. Vij, D. Kumar, P. K. Khanna, M. Kumar, S. Gautam, and K. H. Chae, Semicond. Sci. Technol. **28** (2013).
- 7 D. Thapa, J. Huso, H. Che, M. Huso, J. L. Morrison, D. Gutierrez, M. G. Norton, and L. Bergman, Appl. Phys. Lett. **102** (2013).
- 8 W. Yang, S. S. Hullavarad, B. Nagaraj, I. Takeuchi, R. P. Sharma, T. Venkatesan, R. D. Vispute, and H. Shen, Appl. Phys. Lett. **82**, 3424 (2003).
- 9 David R. Lide, (CRC Press, Boca Raton, FL, 2005).
- 10 William L. Masterson and Cecile N. Hurley, *Chemistry: Principles and Reactions*, Fifth ed. (Thomson Brooks/Cole, Belmont, Ca, 2004).
- 11 M. Wei, R. C. Boutwell, J. W. Mares, A. Scheurer, and W. V. Schoenfeld, Appl. Phys. Lett. **98** (2011).
- 12 E. Iliopoulos, A. Adikimenakis, E. Dimakis, K. Tsagaraki, G. Konstantinidis, and A. Georgakilas, J. of Cryst. Growth **278**, 426 (2005).
- 13 X. Z. Dang, C. D. Wang, E. T. Yu, K. S. Boutros, and J. M. Redwing, Appl. Phys. Lett. **72**, 2745 (1998).
- 14 S. Hullavarad, N. Hullavarad, D. Look, and B. Claflin, Nanoscale Res. Lett. **4**, 1421 (2009).

Other progress in cubic oxides: NiMgO

NiMgO thin films by sol-gel spin coating

While investigating MBE-grown oxides, we also explored lower-cost solution deposition using sol-gel. This work focused on the complementary oxide, NiMgO, and resulted in the first presentation of tunable NiMgO films across the full compositional range. We correlated changing concentration with tuning of the bandgap and explored the relationship between crystallinity and elemental composition as the Mg fraction varied between samples.

This work produced positive results and was published in Thin Solid Films in 2012. Details of the work are below:

Optical and Structural Properties of NiMgO Thin Films Formed By Sol-Gel Spin Coating

Introduction

NiMgO has shown much promise as a material for ultraviolet (UV) detection in recent years due to its wide direct band gap (E_g) and full miscibility across the compositional range[1]. This miscibility from cubic MgO ($E_g = 7.8$ eV) to cubic NiO ($E_g = 3.6$ eV)[2] allows for single phase film growth through the deep UV and into the vacuum UV. In addition, the crystalline mismatch between NiO (4.18 Å) and MgO (4.21 Å) is less than 1%[3], allowing for close lattice matching of the ternary films to MgO substrates[1]. Films grown with distinct band edges in this range may be used as active regions in flame monitoring and combustion detection or as emitters in germicidal UV scrubbers or UV light emitting diodes. While binary NiO is used for catalytic and electrochromic applications and MgO is explored as an insulator, the NiMgO ternary is still relatively unstudied, with only a few articles investigating optical properties in the UV[4-6]. While NiMgO has been investigated using molecular beam epitaxy, e-beam evaporation, and RF magnetron deposited polycrystalline films[2, 7, 8], little effort has been put forth in investigating NiMgO with inexpensive growth techniques such as sol-gel. The sol-gel process allows for the generation of consistent films from inexpensive precursor solutions and is scalable, making it well suited for volume industrial manufacturing. While previous research has investigated dip-coating[9], spin coating the sol has not been studied and may provide unique opportunities for thin film development. Here we report on the UV optical and structural properties of spin coated NiMgO sol-gel films across the entire compositional range. Although NiMgO coatings offer opportunity for visible-transparent applications, in this article we focus on the potential for UV band edge tuning to meet the needs of UV-C optoelectronic devices.

Experimental details

Nickel acetate tetrahydrate ($\text{Ni}(\text{CH}_3\text{CO}_2)_2 \cdot 4\text{H}_2\text{O}$) and magnesium acetate tetrahydrate ($\text{Mg}(\text{CH}_3\text{CO}_2)_2 \cdot 4\text{H}_2\text{O}$) were used as precursor materials for Ni and Mg, respectively, and mixed in solution with 2-methoxyethanol ($\text{C}_3\text{H}_8\text{O}_2$) to form the colloidal suspension. The solution was stirred at 400rpm for 60 minutes while covered and heated to 60°C. The ratio of Ni:Mg precursor material was varied to obtain ternary films of various composition with different absorption edges across the compositional range. Each solution was aged for over 20 hours to produce a low-density gel. The sol-gel was deposited onto quartz substrates loaded into a spin coater. The solution was dispensed onto the substrate and then spun at 5000 rpm for 60 seconds. In order to obtain films of ~250 nm thickness, ten spin coated layers were carried out on each substrate with a 300°C, 10 minute bake and 5 minute cool between each successive spin coating. To determine the appropriate sintering temperature, a set of $\text{Ni}_{0.54}\text{Mg}_{0.46}\text{O}$ films were sintered at three different temperatures – 600°, 800°C, and 1000°C – for 2 hours in air with a flow rate of approximately 1L/min. A MgO film was also produced from an un-aged sol and baked at 400°C between spin coating iterations. The films produced were approximately 125 nm thick, as measured by profilometry, with the exception of the 170 nm thick MgO film. A Veeco Dimension 3100 atomic force microscope (AFM) in tapping mode was used to characterize surface morphology, while a Cary 500 UV-Vis-IR spectrophotometer was used for optical transmission. Crystalline structure and lattice spacing were determined from the copper k-alpha line at 1.54Å using a Rigaku D-max x-ray diffractometer (XRD) with thin film soller slits. Sample composition was investigated using a Physical Electronics 5400 ESCA x-ray photoelectron spectrometer (XPS) using Ar^+ ions with a beam set a 4kV sputtering at 40 A/min. Some preliminary photoluminescence measurements were also taken with a continuous wave 325 nm He-Cd laser.

Results and discussion

Figure 17 shows the transmission data for the $\text{Ni}_{0.54}\text{Mg}_{0.46}\text{O}$ thin films sintered at different temperatures compared to the as-deposited film. Sintering at temperatures up to 800°C resulted in an increase in transparency of the films, particularly for spectral regions below the band edge. Furthermore, the band edge becomes sharper. For sintering at 1000°C, the transparency drops along with a smoothing of the band edge transmission. XRD data from the same films is shown in the inset of Figure 17. A clear peak emerges upon sintering at all temperatures, positioned at a 2θ angle of ~43.25°, consistent with that expected for the $\text{Ni}_{0.54}\text{Mg}_{0.46}\text{O}$ films. This verifies that the films become crystalline during the sintering process, as expected, with an increased crystallinity for higher sintering temperatures. Despite the stronger XRD peak from the NiMgO film sintered at 1000°C however, AFM of the sample indicated a relatively rough surface with a root-mean squared (rms) value of 3.95 nm, in comparison to the < 1nm rms of samples annealed at 600°C (rms=0.58 nm) and 800°C (rms=0.70 nm). This supports the

conclusion that a sintering temperature of 800°C results in smoother films with higher transparency than the 1000°C despite the higher XRD peak intensity for 1000°C.

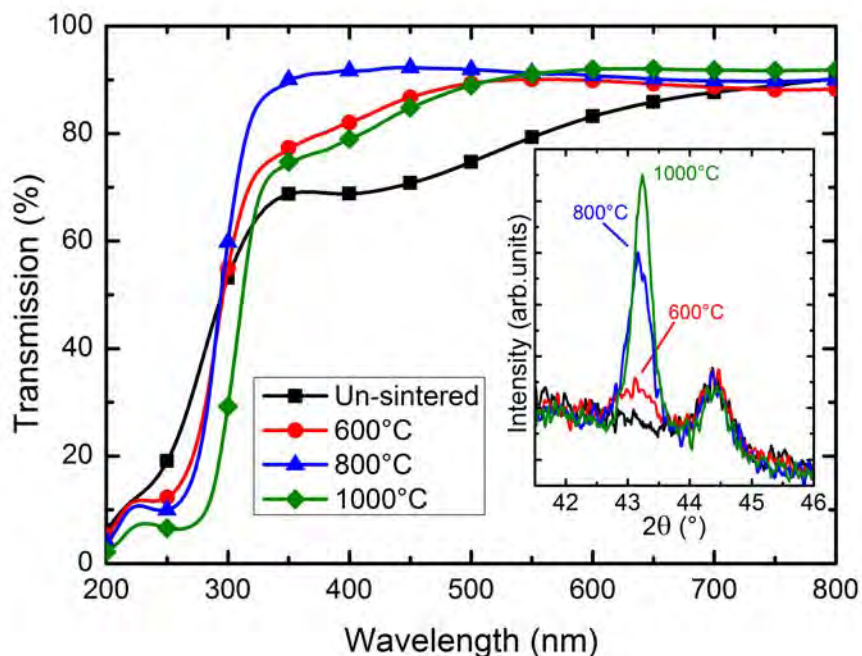


Figure 17: Transmission spectra of as-deposited and sintered of $\text{Ni}_{0.54}\text{Mg}_{0.46}\text{O}$ films. XRD patterns are shown in the inset.

For compositional analysis of films, XPS and Rutherford backscattering (RBS) were used to determine the Ni:Mg ratio in comparison to the sol. Both XPS and RBS were in good agreement, and indicated that the $\text{Ni}_{1-x}\text{Mg}_x\text{O}$ films contain a similar ratio of metal ions as compared to the precursor ratio in the initial sol. This indicates that there is a close correlation between precursor input and film output with the NiMgO sol-gel process, making compositional tuning of the films relatively simple.

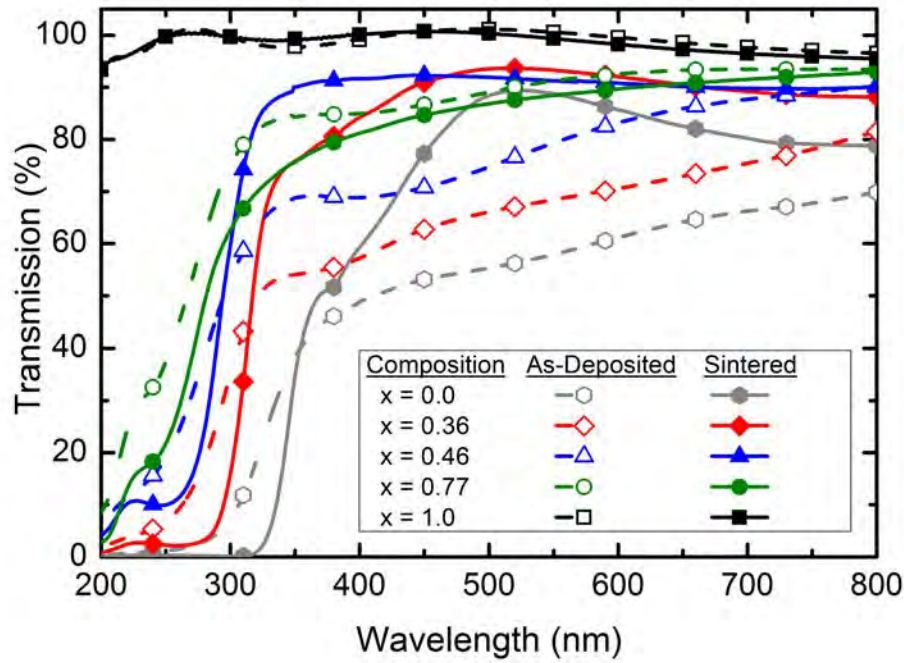


Figure 18: Transmission spectra of as deposited and sintered (800°C) Ni_{1-x}Mg_xO films with Mg content varying from 0 to 1.

Figure 18 shows the potential for band gap tuning with NiMgO polycrystalline films. Here, four films are shown to allow increasingly blue-shifted transmission with increasing Mg content, as anticipated from previously reported NiMgO growth[7-9]. As-deposited films were found to have visible transmission values of 50-80%, but in all cases the sintered transmission quality improves to values above 80%. Ellipsometer measurements (not shown here) indicate sintered NiMgO absorption is low over the visible/near infrared range and the index of refraction is relatively constant. This suggests the change in transmission between unsintered and sintered films may be related to reduced absorption from residual solvent that is removed during the sintering process. The observed absorption edges of the sintered films show a clear shift to shorter wavelengths with increasing Mg concentration, moving from about 300 nm to 200 nm as Mg concentration is adjusted from $x=0.0$ to 0.77. It should be noted that a pure MgO film ($x=1.0$) was also included as prepared, demonstrating a much shorter wavelength transmission edge. However, determination of the exact band edge of the MgO film requires a spectrophotometer operating in vacuum due to absorption in the air below 200nm.

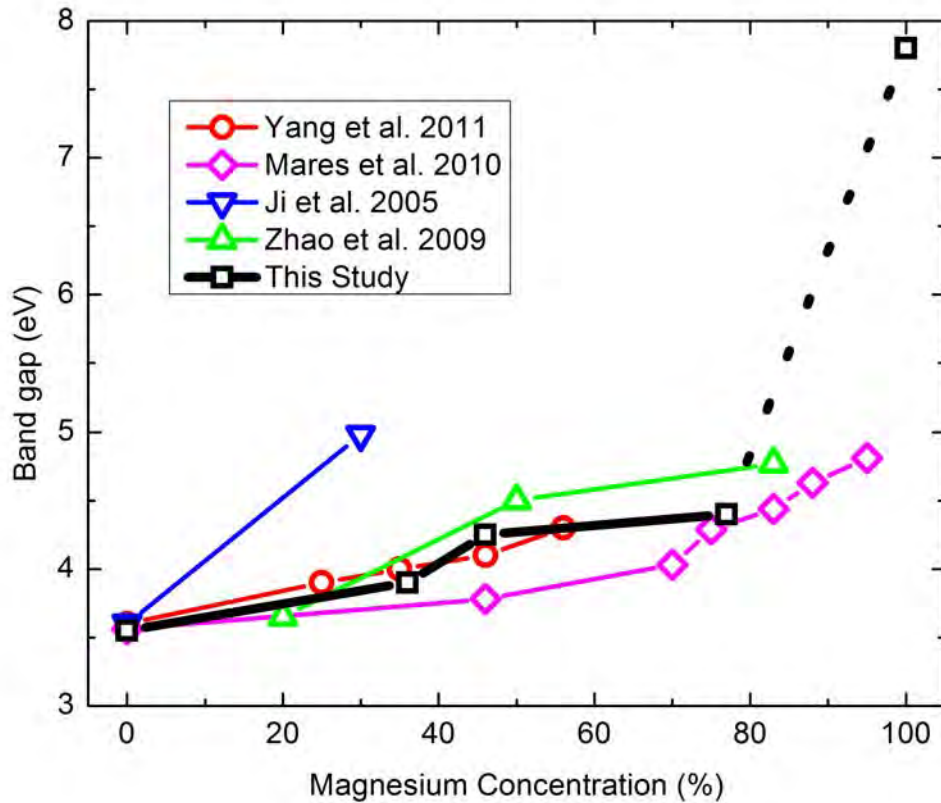


Figure 19: Optical band gap of Ni_{1-x}Mg_xO films with Mg content varying from 0 to at. 100%

Figure 19 provides a comparison of band edges produced in this study to other NiMgO film investigations. There is relatively good agreement in the literature evidencing nonlinearity in the evolution of the ternary band gap. Several reports follow a similar linear trend of increasing energy from about 3.5 to 4.8 eV as Mg concentration is increased, with a discontinuity for pure MgO, at a value of 7.8 eV[1, 8, 10]. This has previously been explained as a microscopic inhomogeneity in the film composition, due to differences in mobility between constituents during formation[7]. However, determining equal chemical potential in all growth methods represented requires rigorous simulation not attempted here. Additionally, microscopic inhomogeneity would suggest the presence of a miscibility gap. However, with similar ionic radii, identical valencies and crystal structures, and the ability to form a solid solution across the range, the origin of a miscibility gap between NiO and MgO is tenuous[11].

An alternative explanation may be related to the origin of the band gap in each of the binaries. The MgO band gap is formed from the 3s state of the anion, which acquires 2 valence electrons from the Mg atom upon forming its ionic bond[12]. This O 3s state forms the conduction band, while the O 2p and 2s states (which are less-tightly bound than the Mg 2p) form the upper and lower valence bands respectively[13]. Alternatively, NiO is a charge-transfer type insulator where band gap is believed to originate from a valence band composed mainly of O 2p states and a conduction band built from hybridization of the Ni 3d and O 2p bands

as impacted by dynamical correlation with the Ni 3d states[14, 15]. It is possible that as these two binaries mix in solution, the band behavior of the ternary is a convolution of these two insulating regimes, resulting in a nonlinearity of band evolution with varying compositions of NiO and MgO.

This nonlinearity may be due instead to oxygen vacancies in the film (as described by F and F⁺ centers previously reported in MgO[16]). Photoluminescence (PL) was also performed on several films (not reported on here) and contained an emission peak near 413nm. A prior study reported this to be related to oxygen defects[17], supporting the suggestion that some of the nonlinearity in observed band edge may be related to differences in oxygen vacancy concentration.

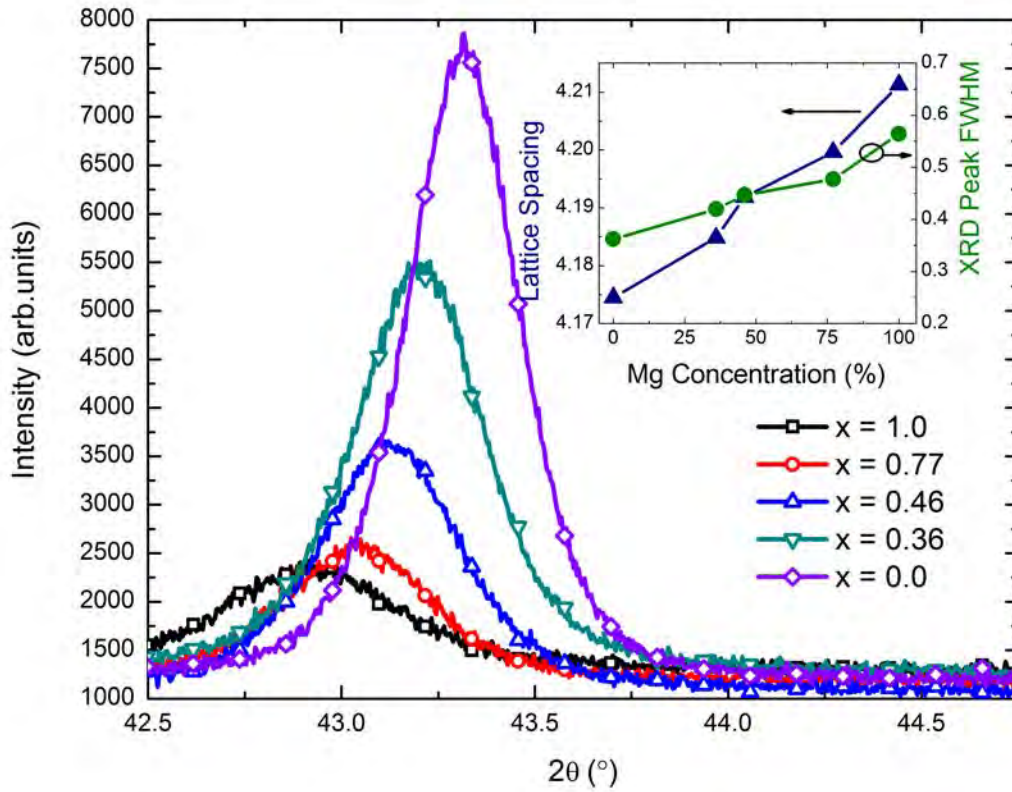


Figure 20: XRD (002) peak for Ni_{1-x}Mg_xO films. FWHM and lattice spacing are shown in the inset with varying Mg content.

The structural properties of the NiMgO sol-gel films were investigated by XRD. Figure 20 provides XRD data for each of the different film concentrations produced. A linear shift in lattice parameter was observed as Mg concentration in the film was increased, summarized in the inset in Figure 20, following Vegard's Law[18]. We also observe a continuous increase in XRD peak full width at half maximum (FWHM) with increasing Mg concentration as shown in the inset, suggesting reduced orientation and smaller grains with increasing Mg composition. While diffracted intensity also appears to increase with increasing Ni incorporation, this is largely due to increased scattering off of the Ni atom, as it has a higher atomic number than Mg.

Summary

NiMgO films across the full compositional range were synthesized by a low-cost sol-gel process with <1nm rms roughness for sintering temperatures of 800°C. XPS and RBS data indicated that the Mg:Ni ratio of precursors was maintained in the sol-gel films after sintering, allowing for simple adjustment of film concentration and associated properties. Resultant films were found to have a linear band edge shift with Mg concentration, adjustable from 3.5 to 4.4 eV as Mg concentration was increased from $x=0.0$ to 0.77. A discontinuity in band edge was found for pure MgO, correlating with several other reports, and possibly due to oxygen vacancies in the films. Additionally, XRD data showed increasing atomic spacing and increasing peak FWHM with increased Mg incorporation, following Vegard's Law and suggesting improved orientation in Ni rich films. This study demonstrates the ability to tune the band edge of sol-gel synthesized NiMgO through adjustment of alloy composition, suggesting that such films may offer a low-cost route towards realizing ultraviolet optoelectronic devices.

References

- [1] J.W. Mares, R.C. Boutwell, A. Scheurer, M. Falanga, W.V. Schoenfeld, in: F.H. Teherani, D.C. Look, C.W. Litton, D.J. Rogers (Eds.), *Oxide-based Materials and Devices*, San Francisco, U.S.A., January 24, 2010, SPIE Photonics West, (2010) 76031B.
- [2] J.W. Mares, R.C. Boutwell, M. Wei, A. Scheurer, W.V. Schoenfeld, *Appl. Phys. Lett.* 97/16 (2010) 161113.
- [3] E. Cazzanelli, A. Kuzmin, N. Mironova-Ulmane, G. Mariotto, *Phys. Rev. B* 71/13 (2005) 134415.
- [4] O.I. Goncharova, T.M. Yurieva, *React. Kinet. and Catal. Letters* 15/1 (1980) 73.
- [5] E.O. Zayim, I. Turhan, F.Z. Tepehan, N. Ozer, *Sol. Energy Mater. and Sol. Cells* 92/2 (2008) 164.
- [6] C. Bondoux, P. Prene, P. Belleville, F. Guillet, S. Lambert, B. Minot, R. Jerisian, *Mater. Sci. in Semicond. Process.* 7/4-6 (2004) 249.
- [7] Y.M. Zhao, J.Y. Zhang, D.Y. Jiang, C.X. Shan, Z.Z. Zhang, B. Yao, D.X. Zhao, D.Z. Shen, *J. Phys. D-Appl. Phys.* 42/9 (2009) 092007.
- [8] Z.-G. Yang, L.-P. Zhu, Y.-M. Guo, Z.-Z. Ye, B.-H. Zhao, *Thin Solid Films* 519/15 (2011) 5174.
- [9] Z.G. Ji, Z.P. He, K. Liu, S.C. Zhao, Z.J. He, *J. Cryst. Growth* 273/3-4 (2005) 446.
- [10] W.V. Schoenfeld, M. Wei, R.C. Boutwell, J.W. Mares, A. Scheurer, *Appl. Phys. Lett.* 98/26 (2011) 261913.
- [11] J.S. Choi, H.Y. Lee, K.H. Kim, *J. Phys. Chem.* 77/20 (1973) 2430.
- [12] P.K. de Boer, R.A. de Groot, *J. Phys. Condens. Matter* 10/45 (1998) 10241.
- [13] S.A. Canney, V.A. Sashin, M.J. Ford, A.S. Kheifets, *J. Phys. Condens. Matter* 11/39 (1999) 7507.
- [14] X. Ren, I. Leonov, G. Keller, M. Kollar, I. Nekrasov, D. Vollhardt, *Phys. Rev. B* 74/19 (2006) 195114.
- [15] O. Miura, T. Fujiwara, *Phys. Rev. B* 77/19 (2008) 195124.

- [16] Y. Chen, J.L. Kolopus, W.A. Sibley, Phys. Rev. 186/3 (1969) 865.
- [17] S. Mochizuki, T. Saito, Physica B-Condens. Matter 404/23-24 (2009) 4850.
- [18] A.R. Denton, N.W. Ashcroft, Phys. Rev. A 43/6 (1991) 3161.

Ozone Source Investigation

Our group has pioneered wide bandgap cubic and wurtzite oxide semiconductor growth for several years under multiple Army funded projects. In all prior projects, we have utilized an oxygen plasma source for molecular beam epitaxy (MBE) growth of our epitaxial layers. We have a SVT Associates ozone source in place within our lab that is currently operational and available for use on our MBE system, but to date have not yet determined its value to our Army projects and MBE oxide growth in comparison to the current oxygen plasma source. Under this program we aimed to develop an ozone-based MBE growth capability for c- and w-MgZnO with the goal of determining the benefits/value of an ozone system over the current oxygen plasma source for oxide MBE growth. While there are many purported benefits of ozone sources, one of the most interesting for us is the growth rate. Our typical growth rates are $\sim 0.2 \mu\text{m/hr}$ for our highest quality c- and w-MgZnO layers. As shown in Figure 21 (see inset in (b)), we have identified a direct correlation to the PL lifetime and growth rate for our wurtzite films.

This indicates that we should expect increased PL lifetime, and reduced point defects, in our epilayers if we are able to increase the typical growth rates. This would also have a significant impact on the economics of oxide MBE growth since increasing the growth rate will result in a higher throughput for epilayer growth. To date, little information is available for ozone oxide MBE growth, with most of the prior work being done in Japan (i.e. non-domestically). It is our belief that to maintain U.S. technical position in oxide MBE, an assessment of the value and benefits of ozone based MBE growth needs to be undertaken, as proposed in this project. The following section provides some details of our past work on optimizing oxygen plasma growth and resultant films/devices in both cubic and wurtzite films, validating our ability to carry out the proposed work.

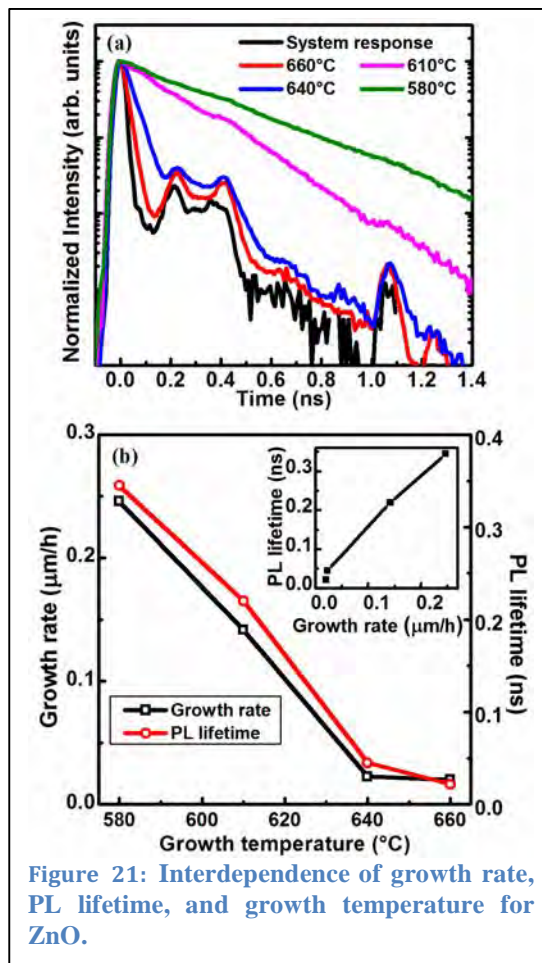


Figure 21: Interdependence of growth rate, PL lifetime, and growth temperature for ZnO.

Hardware Preparations

Under the project we utilized a new oxygen resistant Zn effusion cell that was purchased from SVT Associates (SVTA) in Eden Prairie, MN. Figure 22 provides an image of the source shown installed to the growth chamber.



Figure 22. Photograph of the installed oxygen resistant Zn source on the MBE growth system.

We were also successful in completing the installation of the ozone generation system on the MBE. Initial work focused on locating the ozone system adjacent to the MBE system in a suitable position, as shown in Figure 23.



Figure 23. Photograph of the ozone system, positioned adjacent to the MBE system.

We discovered the need for installation of additional power outlets due to safety requirements about extension cords in the lab. This was carried out by university facilities, as required, and the proper power was put in place for the system to meet fire and safety codes. We then arranged a visit by Ralf Hartmann from SVTA to come and verify that the system was operational. We were successful in generating ozone with the system as it is designed, but did not send this into the growth

chamber due to the need to obtain a larger diameter stainless line from the ozone system to the injector on the MBE system. The current line was $\frac{1}{4}$ " diameter, and it was recommended that we increase to a $\frac{1}{2}$ " diameter line to reduce pre-reaction of generated ozone as it is delivered to the MBE injector. Following the recommendation, we drew up a diagram for a $\frac{1}{2}$ " diameter stainless line with the proper fittings and also decided to incorporate an ozone optical monitoring system into the source line to the injector, and procured the line.

Figure 24 shows an image of the source line we installed that connects the generator to the injector on the MBE system. The inset highlights the inline ozone optical monitoring system that is capable of qualitatively monitoring the level of ozone being delivered to the MBE injector. This is a very valuable metrology tool given that it can assist in ensuring we utilize similar ozone delivery conditions during growth, much like a flux monitor ensures that source flux is equivalent to prior levels.

Figure 24. Photograph of the source line from the ozone system to the MBE system. Also shown is the inline ozone monitoring system that was installed to help monitor ozone delivery during operation.

We then carried out multiple test runs of the ozone generation and were able to verify that the system was producing a measurable amount of ozone. This was primarily clear due to the ozone sensor within the system cabinet that indicated elevated ozone present in the cabinet. Our next step was to attempt ZnO growth on sapphire substrates.

Growth Efforts with Ozone Source

Efforts to nucleate and grow ZnO proved rather challenging, with most growths only resulting in limited ZnO that was too thin to measure. Dr. Liu carried out roughly 20 growth efforts under various ozone generation growth conditions, but was not able to identify a suitable set of conditions that gave acceptable ZnO. Originally we had planned on having several months of growth optimization, but the ozone system hardware proved challenging to integrate into the MBE system and required considerable repair and re-design in collaboration with SVTA and Agnitron, causing a significant delay in the start of the growth effort. As a result, the project ended after just about 6 weeks of growth effort. We were not able to determine if the challenges in demonstrating satisfactory ZnO growth by ozone were due to hardware issues or simply lack of identifying the appropriate growth conditions. The ozone optical measurement appears to indicate that sufficient ozone is being generated, but we do not have a satisfactory method for determining how much of the generated active ozone is making it to the substrate for growth. It appears as though there are still some challenges in delivering the appropriate concentration of ozone for growth, likely requiring additional evaluation of the ozone injector in the system port and its effectiveness in delivering the proper amount of ozone to the growth surface. We remain optimistic based on reports out of Japan that ozone

based ZnO growth can yield high quality ZnO, but now see the need for an extended effort in hardware development and validation to ensure proper ozone delivery in the MBE system.

Future work and potential direction

The wide bandgap oxide work presented here was the culmination of nearly four years of vigorous research. In addition to discovering surface-type behavior of gallium doped MgO and pioneering sol-gel NiMgO, significant advances were made in cubic ZnMgO UV sensors. Despite the challenge presented in extrinsic doping of these films, optimization of growth parameters and device fabrication resulted in dramatic improvement in oxide UV sensing and thin film oxide research. In addition to the technical advancements realized under the program, the project also directly supported (partially or fully) the PhD dissertation work that resulted in successful graduation of three PhD students.

There exists a broad opportunity for future advancement in oxide thin film detectors through continued refinement in process and advancement in device design. The work carried out in this program focused on oxide growth by oxygen plasma and exploring how these materials growth conditions impacted the ultimate performance of fabricated devices from the resultant films. An ozone generating source has recently been connected to the MBE reactor, opening up a new facet of potential materials development of the ternary cubic oxides that may have a significant advancement on the performance and quality of solar-blind detectors. While initial efforts were put forth to identify suitable ozone growth conditions for ZnO, they were very limited and future work under new agreements would be necessary to properly determine the benefits of using an ozone source for oxygen. Of particular interest is if it enables a higher quality of oxide films that realize increased responsivity while reducing any persistent photoconductivity, enabling a higher level of performance. Additionally, given the challenges of extrinsic doping in these oxides, it would be valuable to enlist the help of a theorist who can guide us on what elements and extrinsic doping schemes appear most probable for realizing p- and n-type doping. Lastly, given the current performance of demonstrated devices, an accurate assessment of their performance in comparison to other available devices should be undertaken to determine their suitability for commercialization.